

1                   **Synchronous emplacement of the anorthosite  
2                   xenolith-bearing Beaver River diabase and one of the  
3                   largest lava flows on Earth**

4                   **Yiming Zhang<sup>1</sup>, Nicholas L. Swanson-Hysell<sup>1</sup>, Mark D. Schmitz<sup>2</sup>, James D.  
5                   Miller Jr.<sup>3</sup>, Margaret S. Avery<sup>1,4</sup>**

6                   <sup>1</sup>Department of Earth and Planetary Science, University of California, Berkeley, CA, USA

7                   <sup>2</sup>Department of Geosciences, Boise State University, Boise, ID, USA

8                   <sup>3</sup>Department of Earth and Environmental Sciences, University of Minnesota, Duluth, MN, USA

9                   <sup>4</sup>Geology, Minerals, Energy, and Geophysics Science Center, U.S. Geological Survey, Moffett Field, CA,  
10                   USA

11                   **Key Points:**

- 12                   • New geochronology on an anorthosite xenolith tightly constrain the timing of the  
13                   Beaver River diabase intrusions.
- 14                   • Paleomagnetic and geochronological data support that the Beaver River diabase  
15                   is comagmatic with the very high volume Greenstone Flow.
- 16                   • Wide conduits of magma to the surface are indicated by large anorthosite xeno-  
17                   liths.

18 **Abstract**

19 New geochronologic and paleomagnetic data from the North American Midcontinent Rift  
 20 (MCR) reveal the synchronous emplacement of the Beaver River diabase, the anorthosite  
 21 xenoliths within it, and the Greenstone Flow — one of the largest lava flows on Earth.  
 22 A U-Pb zircon date of  $1091.83 \pm 0.21$  Ma ( $2\sigma$ ) from one of the anorthosite xenoliths is  
 23 consistent with the anorthosite cumulate forming as part of the Midcontinent Rift and  
 24 provides a maximum age constraint for the Beaver River diabase. Paired with the min-  
 25 imum age constraint of a cross-cutting Silver Bay intrusion ( $1091.61 \pm 0.14$  Ma;  $2\sigma$ ) these  
 26 data tightly bracket the age of the Beaver River diabase to be  $1091.7 \pm 0.2$  Ma (95% CI),  
 27 coeval with the eruption of the Greenstone Flow ( $1091.59 \pm 0.27$  Ma;  $2\sigma$ ) — which is  
 28 further supported by indistinguishable tilt-corrected paleomagnetic pole positions. Geochrono-  
 29 logical, paleomagnetic, mineralogical and geochemical data thus support the hypothe-  
 30 sis that the Beaver River diabase was the feeder system for the Greenstone Flow. The  
 31 large areal extent of the intrusives and large estimated volume of the volcanics suggest  
 32 that they represent a rapid and voluminous *ca.* 1092 Ma magmatic pulse near the end  
 33 of the main stage of MCR magmatism.

34 **1 Introduction**

35 The North American Midcontinent Rift (MCR) is a *ca.* 1.1 Ga large igneous province  
 36 for which there is excellent exposure of both the intrusive and extrusive components in  
 37 the Lake Superior region (Fig. 1). An exceptional feature within the Midcontinent Rift  
 38 is the occurrence of large anorthosite xenoliths within a diabase sill and dike network  
 39 known as the Beaver River diabase that outcrops in northeastern Minnesota, USA, as  
 40 part of the Beaver Bay Complex (Fig. 1). The anorthosite xenoliths range in size from  
 41 centimeter-scale megacrysts to meter-scale, decimeter-scale and even  $>150$  meter-scale  
 42 blocks (Fig. 2; Morrison et al. (1983); Grout (1939)). A particularly large anorthosite  
 43 xenolith is exposed at Carlton Peak in the eastern Beaver Bay Complex with minimum  
 44 dimensions of  $180 \times 240$  meters (Fig. 1, 2; Boerboom et al. (2006)). In the southern Beaver  
 45 Bay Complex, a large anorthosite xenolith near Corundum Point has dimensions of  $180$   
 46  $\times 230$  meters while the one exposed at Split Rock Point has dimensions of  $180 \times 260$   
 47 meters (Boerboom, 2004). To be able to accommodate such large xenoliths during magma  
 48 ascent from the lower crust, the Beaver River diabase conduits must have been of at least  
 49 the width of the anorthosite short axis diameters. Such wide conduits in these near-surface

intrusions suggest high magma flux rates and make it likely that the magma extruded to the surface — feeding voluminous lava flows.

Miller and Chandler (1997) emphasized the composite nature of the Beaver River diabase network and Silver Bay intrusions (Fig. 1), which are locally marked by abrupt transitions to progressively more evolved lithologies. Furthermore, that study documented geochronologic, geochemical and structural evidence to support the notion that the diabase network may have served as principal feeder conduits to lava flows including parts of the Portage Lake Volcanics on the Keweenaw Peninsula and Isle Royale of Michigan (Fig. 1). To more directly test this inferred intrusive-extrusive correlation, Doyle (2016) compared the mineralogical, textural, and geochemical attributes and the composite lithologic nature of the Beaver River diabase against those of the Greenstone Flow, the largest lava flow within the Midcontinent Rift and one of the largest lava flows on Earth (Fig. 3). The Greenstone Flow also has a composite nature, which is indicated by its lithologic zonation of ophitic basalt forming the upper and lower zones and an interior zone composed of prismatic ferrogabbro to granophyric monzodiorite. Doyle (2016) documented remarkable similarities in petrography, mineral chemistry, whole rock geochemistry, and lithologic zonation between the Beaver River diabase intrusions in northern Minnesota and the Greenstone Flow on both Isle Royale and Keweenaw Peninsula. Based on the interpreted feeder system being in northern Minnesota, Doyle (2016) estimated the full extent of the Greenstone Flow to be  $\sim 20000 \text{ km}^2$  and its volume to be between 2000 and 6000  $\text{km}^3$  (Fig. 3).

A comagmatic relationship between the Beaver River diabase and the Greenstone Flow is consistent with the similar  $^{207}\text{Pb}/^{206}\text{Pb}$  dates developed from a granophyric ferrogabbro within the Beaver Bay Complex ( $1095.8 \pm 1.2 \text{ Ma}$ , Paces and Miller (1993)) and the Greenstone Flow ( $1094.0 \pm 1.5 \text{ Ma}$ , Davis and Paces (1990)). The relatively large uncertainties provided by the existing  $^{207}\text{Pb}/^{206}\text{Pb}$  geochronology more roughly constrains the temporal relationships between these rapid events than is possible with modern methods. Modern-day U-Pb geochronology techniques for chemical abrasion isotope dilution-thermal ionization mass spectrometry (CA-ID-TIMS) allow high precision  $^{206}\text{Pb}/^{238}\text{U}$  dates to be developed from chemically-abraded zircon crystals (Mattinson, 2005). Studies utilizing these methods on Midcontinent Rift volcanics and intrusions have shown that the analytical uncertainties on weighted mean  $^{206}\text{Pb}/^{238}\text{U}$  dates of multiple chemically-abraded single zircons can be of  $\sim 200 \text{ kyr}$ , an order of magnitude smaller than previ-

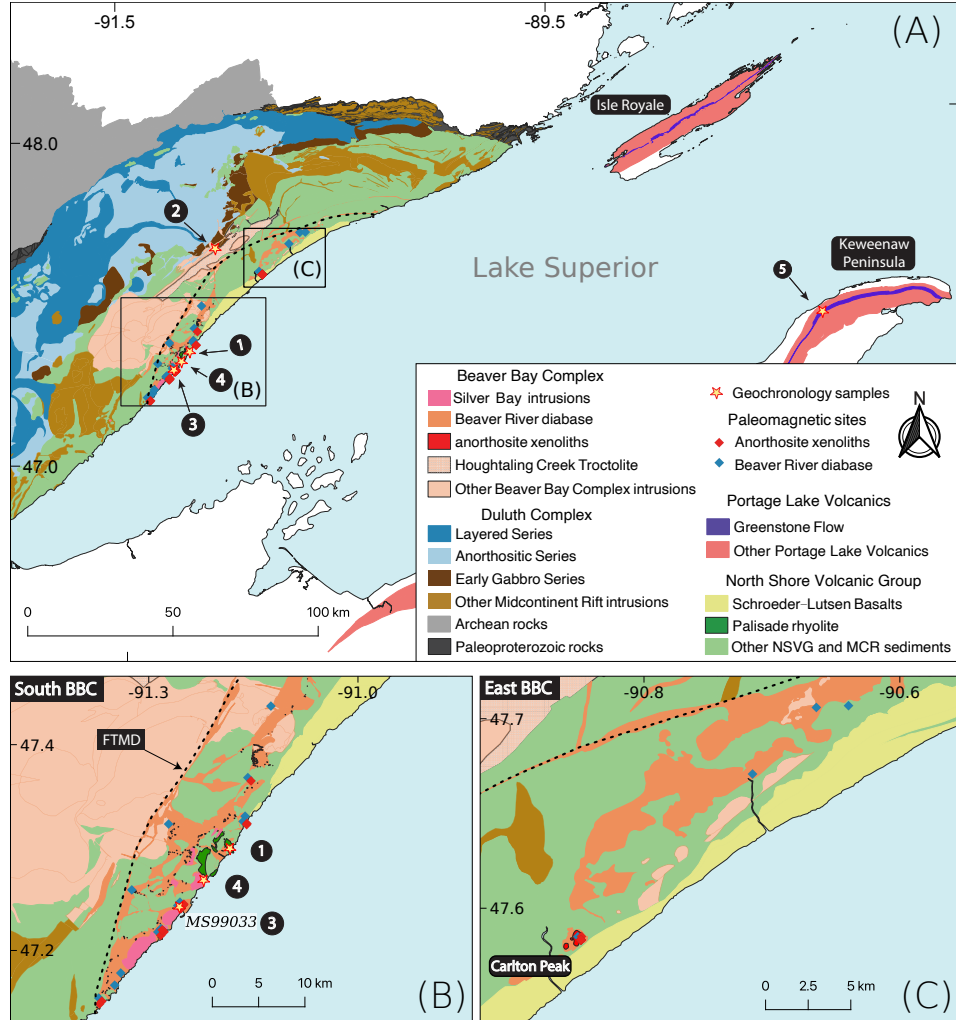


Figure 1: (A) Geologic map of exposures of Midcontinent Rift volcanics and intrusives in the western Lake Superior region. The Greenstone Flow (purple) of the Portage Lake Volcanics (red) outcrops throughout the Keweenaw Peninsula and Isle Royale. (B) Regional map of paleomagnetic and geochronologic sites in the southern Beaver Bay Complex (south BBC). Note that paleomagnetic site AX16 and geochronology sample MS99033 are from the same anorthosite xenolith. The geochronology sample numbers in (A) and (B) correspond to those in Fig. 4. (C) Regional map of paleomagnetic sites in the eastern Beaver Bay Complex (east BBC). The xenolith at Carlton Peak is >100 meters in diameter. The younger Schroeder-Lutsen basalt of the North Shore Volcanic Group (NSVG) is lying unconformably atop the Beaver River diabase and other NSVG units. The nomenclature of the “southern” and “eastern” Beaver Bay Complex follows Miller and Chandler (1997). FTMD - Finland tectonomagmatic discontinuity, traced out by the dashed black line. Bedrock geology is from Miller et al. (2001) and Jirsa et al. (2011).

83       ous dates that are based exclusively on the  $^{207}\text{Pb}/^{206}\text{Pb}$  system (Fairchild et al., 2017;  
 84       Swanson-Hysell et al., 2019, 2020). These  $^{206}\text{Pb}/^{238}\text{U}$  dates are also considered to be more  
 85       accurate than systematically older  $^{207}\text{Pb}/^{206}\text{Pb}$  dates (Schoene et al., 2006). Such  $^{238}\text{U}/^{206}\text{Pb}$   
 86       dates have revealed that the massive Layered Series and Anorthositic Series rocks of the  
 87       Duluth Complex were emplaced in  $\sim$ 500 kyr *ca.* 1096 Ma (Swanson-Hysell et al., 2020).

88       In this work, we use a new  $^{206}\text{Pb}/^{238}\text{U}$  zircon date for an anorthosite xenolith within  
 89       the Beaver River diabase, in conjunction with  $^{206}\text{Pb}/^{238}\text{U}$  dates from a Silver Bay in-  
 90       trusion and the Greenstone Flow (Fig. 1; Fairchild et al. (2017)), to evaluate the tim-  
 91       ing of emplacement of the Beaver River diabase, and the hypothesized intrusive-extrusive  
 92       correlation between the Beaver River diabase and the Greenstone Flow.

93       Paleomagnetic data can also provide chronological constraints on rock units. Lau-  
 94       rentia experienced a period of rapid latitudinal plate motion during rift development (Swanson-  
 95       Hysell et al., 2009). A synthesized apparent polar wander path (APWP) based on the  
 96       Midcontinent Rift volcanic rocks indicates that motion exceeded 20 cm/yr (Swanson-  
 97       Hysell et al., 2019), faster than the maximum speed of India of  $\sim$ 17 cm/yr during the  
 98       Cenozoic (van Hinsbergen et al., 2011). This motion resulted in significant differences  
 99       in pole positions recorded by Midcontinent Rift rocks that were emplaced a few million  
 100      years apart (Swanson-Hysell et al., 2019). In this study, we present paleomagnetic data  
 101      from the anorthosite xenoliths and the host Beaver River diabase. Data from the xeno-  
 102      liths give equivalent directions to the host diabase (Figs. 7, 8), indicating that they were  
 103      heated above the Curie temperature of magnetite and acquired a thermal remanent mag-  
 104      netization when they cooled within the diabase. This thermal history is consistent with  
 105      thermal diffusion modeling of the xenoliths (Fig. 9). The paleomagnetic data can be com-  
 106      pared to data from the Greenstone Flow to further test the hypothesis that they are syn-  
 107      chronous. The resulting paleomagnetic pole positions can also be compared to the syn-  
 108      thesized Laurentia APWP to obtain chronological constraints (Fig. 8).

109       Here, by integrating the geochronologic and paleomagnetic perspectives with pre-  
 110       vious lithologic and geochemical analyses (Miller & Chandler, 1997; Doyle, 2016), we more  
 111       definitely establish that the Beaver River diabase network acted as the feeder system for  
 112       the Greenstone Flow of the Portage lake Volcanic-equivalent flows. Their shared geochem-  
 113       ical signatures, composite nature of emplacement, and the inference of giant magma con-

114 ducts that transported large anorthositic xenoliths characterize a period of *ca.* 1092 Ma  
 115 voluminous magmatic activity (based on  $^{206}\text{Pb}/^{238}\text{U}$  zircon dates; Fig. 1).

116 **2 Geologic Setting**

117 **2.1 Beaver Bay Complex and Related Rocks of NE Minnesota**

118 The North American Midcontinent Rift (MCR) is a failed intracontinental rift where  
 119 protracted magmatic activity lasted from *ca.* 1109 Ma to *ca.* 1084 Ma (Swanson-Hysell  
 120 et al., 2019). Midcontinent Rift rocks extensively outcrop in today's Lake Superior re-  
 121 gion, with the total extent traceable by arcuate magnetic and gravity anomalies that ex-  
 122 tend to the southwest to Kansas, and to the southeast, to southern Michigan (Hinze &  
 123 Chandler, 2020). Previous studies have divided magmatic activity in the rift into four  
 124 stages based on interpreted changes in relative magmatic volume and the nature of mag-  
 125 matism: early ( $\sim$ 1109–1104 Ma), latent ( $\sim$ 1104–1098 Ma), main ( $\sim$ 1098–1090 Ma) and  
 126 late ( $\sim$ 1090–1083 Ma) (Vervoort et al., 2007; Heaman et al., 2007; Miller & Nicholson,  
 127 2013). In northeastern Minnesota, the Early Gabbro Series and the Felsic Series rocks  
 128 of the Duluth Complex and reversed-polarity lavas of the lower North Shore Volcanic  
 129 Group were emplaced during the early stage. The more voluminous Duluth Complex Lay-  
 130 ered Series and the plagioclase-rich Anorthositic Series, together with an associated  $\sim$ 8  
 131 km thick extrusive volcanic sequences of the North Shore Volcanic Group (NSVG), were  
 132 rapidly emplaced about 10 myr later at *ca.* 1096 Ma during the main stage (Paces & Miller,  
 133 1993; Swanson-Hysell et al., 2020).

134 The Beaver Bay Complex, which sits stratigraphically above the Duluth Complex,  
 135 is another intrusive complex that resulted from main stage magmatism. The exposed  
 136 area of the Beaver Bay Complex is  $\sim$ 1000 km $^2$  where it has been mapped along the north-  
 137 western shore of Lake Superior in northeastern Minnesota (Fig. 1; Supporting Informa-  
 138 tion). The Beaver Bay Complex is a multi-phase, composite intrusive complex that in-  
 139 trudes parts of the NSVG (Fig. 1; Miller and Chandler (1997); Swanson-Hysell et al. (2020)).  
 140 Distinct from the deep plutonic intrusions of the Duluth Complex, the majority of the  
 141 Beaver Bay Complex is formed of hypabyssal intrusions that were emplaced as dikes and  
 142 sills at shallow depths (Miller & Chandler, 1997). Detailed mapping and petrological anal-  
 143 yses of the Beaver Bay Complex have led to the identification of thirteen intrusive units  
 144 and at least six major intrusive events (Miller & Chandler, 1997). Most of the Beaver

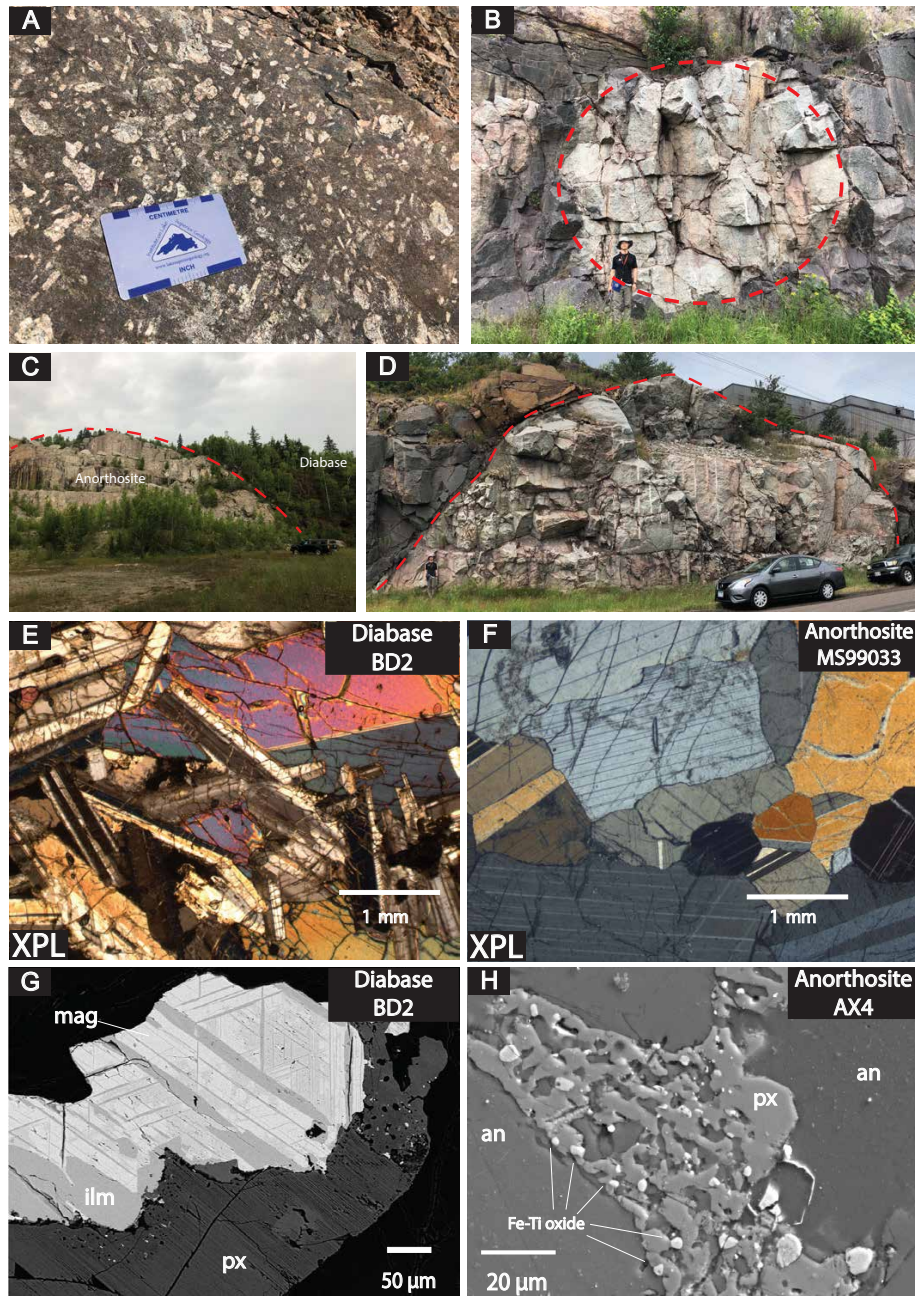


Figure 2: Field photographs and petrographic images of the Beaver River diabase and the anorthosite xenoliths within it. (A) Centimeter-sized plagioclase megacrysts in the diabase. (B) Rounded anorthosite xenolith with a diameter of  $\sim 7$  meters fully entombed within the diabase. (C) Exposure of a giant Carlton Peak anorthosite with a diameter  $>100$  m. (D) 27.5 m diameter anorthosite xenolith sampled as paleomagnetic site AX16 and geochronology sample MS99033. (E) Cross polarized (XPL) image of the subophitic texture of diabase at site BD2 (pyroxene partially enclosing plagioclase). (F) XPL image of anorthosite geochronology sample MS99033. Plagioclase crystals exhibit both granoblastic texture and interlocking lath fabrics. (G) Back scattered electron (BSE) image of a large Fe-Ti oxide with titanomagnetite-ilmenite lamellae in Beaver River diabase site BD2. (H) BSE image of micron-sized Fe-Ti oxides exsolved from pyroxene between plagioclase crystals in anorthosite xenolith site AX4.

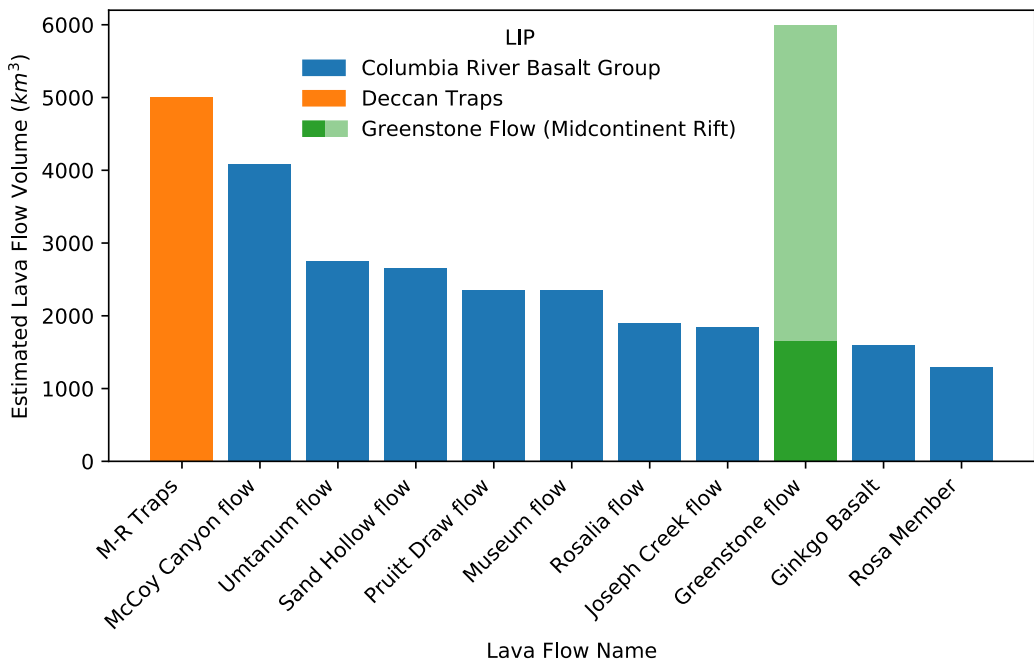


Figure 3: Bar plot of ten of the world's most voluminous single mafic lava flows currently known. With an estimated minimum volume of  $\sim 1650 \text{ km}^3$  and likely volume as high as  $\sim 6000 \text{ km}^3$ , the Greenstone Flow from the 1.1 Ga Midcontinent Rift stands amongst the giant lava flows from the Deccan Traps and Columbia River basalts. M-R Traps = Mahabaleshwar–Rajahmundry lava flow in the Deccan Traps. Volume estimates from Self et al. (2008), Bryan et al. (2010), Longo (1984), and Doyle (2016).

145 Bay Complex intrusions are dioritic to gabbroic in composition (Miller & Chandler, 1997).  
 146 The main lithology of the Beaver River diabase dikes and sills network within the Beaver  
 147 Bay Complex is an ophitic olivine gabbro (Fig. 2), but in wider areas of dikes and the  
 148 upper parts of thick sills, this rock type can abruptly transition into intergranular olivine  
 149 oxide gabbro, then to subprismatic (and commonly foliated) ferrogabbro, and finally to  
 150 granophyric monzodiorite. The more evolved and later emplaced components of the Beaver  
 151 River diabase network are commonly distinguished as the Silver Bay intrusions in the  
 152 southern Beaver Bay Complex (Fig. 1). Overall being intermediate in composition, the  
 153 Silver Bay intrusions lithologies range from ophitic olivine gabbro to ferrogranite (Shank,  
 154 1989). Field mapping by Miller et al. (1994) found intrusive relationship between the Sil-  
 155 ver Bay intrusions and the Beaver River diabase. Angular inclusions of the host Beaver  
 156 River diabase within marginal zones of the Silver Bay intrusions led Miller and Chan-

157 dler (1997) to interpret that the Silver Bay intrusions intruded after the diabase crys-  
 158 tallized.

159 One distinctive feature of the Beaver River diabase is its inclusions of anorthosite  
 160 xenoliths. In the southern part of the Beaver Bay Complex, the Beaver River diabase  
 161 occurs as dikes and sills, typically including anorthosites with various sizes ranging from  
 162 centimeters to over 150 meters (Figs. 1, 2; Grout (1939); Morrison et al. (1983)). The  
 163 diabase in this region intrudes the Palisade rhyolite of the North Shore Volcanic Group  
 164 (Fig. 1), which has a  $^{206}\text{Pb}/^{238}\text{U}$  date of  $1093.94 \pm 0.28$  Ma ( $2\sigma$  analytical uncertainty  
 165 is presented for CA-ID-TIMS dates throughout this work; Swanson-Hysell et al. (2019)).  
 166 The Beaver River diabase is locally intruded by the Silver Bay intrusions (Fig. 1). An  
 167 aplite unit within the granophyre zone of one of these Silver Bay intrusions has a  $^{206}\text{Pb}/^{238}\text{U}$   
 168 date of  $1091.61 \pm 0.14$  Ma (Swanson-Hysell et al., 2019). Another arcuate, sill-like di-  
 169 abase body mapped as the Beaver River diabase outcrops along the eastern part of the  
 170 complex (Fig. 1; Miller and Chandler (1997)). The diabase composition there is simi-  
 171 lar to that in the south and it also contains large anorthosite xenoliths that exceed 100  
 172 meters at Carlton Peak (Fig. 1). The Beaver River diabase in the northern part of the  
 173 complex near the Houghtaling Creek area typically forms narrow, near-vertical dikes in-  
 174 stead of sheets in the southern and eastern regions (Fig. 1; Miller et al. (1994)). The di-  
 175 abase in this region only locally contains xenoliths of anorthosite at dike margins.

176 Hundreds of anorthosite xenoliths have been recognized and mapped within the  
 177 Beaver River diabase (Fig. 1). Many hill tops in the Beaver Bay Complex, such as the  
 178 Carlton Peak and Britton Peak, are large anorthosite blocks (which lead Lawson (1893)  
 179 to erroneously conclude that they were relict Archean topography). Later work estab-  
 180 lished the anorthosite blocks as xenoliths, which are now extensively documented through  
 181 geologic mapping of the region (Fig. 1; Miller et al. (2001); Miller (1988); Miller and Boer-  
 182 boom (1989); Boerboom (2004); Boerboom and Green (2006); Boerboom et al. (2006,  
 183 2007)) and outcrop-scale exposures (Fig. 2). In the field, the anorthosites typically ap-  
 184 pear as subrounded to rounded, light-colored, translucent blocks that are in sharp con-  
 185 tact with the hosting diabase (Fig. 2). They also occur as exposures whose contact with  
 186 the diabase is covered (Fig. 2). Grout (1939) suggested that the rounded anorthosites  
 187 are the result of friction during transportation as they were liberated by the diabase (i.e.  
 188 physical weathering within a magmatic system). While the Beaver River diabase is chilled  
 189 against the North Shore Volcanic Group lithologies that it intrudes, the diabase is not

190 chilled against the margin of the anorthosite xenoliths (Morrison et al., 1983; Miller &  
 191 Chandler, 1997). The lack of chilled contacts is consistent with the anorthosite being at  
 192 elevated temperatures and cooling at the same time as the diabase magma (Fig. 9).

193 The anorthosite xenoliths are dominantly monomineralic plagioclase that has an  
 194 average anorthite content of ~70% (Morrison et al., 1983; Doyle, 2016). Interstitial py-  
 195 roxene and olivine are present in minor concentrations in the xenoliths. Within the Carlton  
 196 Peak anorthosite xenolith, up to 10 cm oikocrysts of altered mafic minerals such as  
 197 olivine can occur. Nevertheless, the overall olivine content in the anorthosites is low. In-  
 198 terstitial titanomagnetite-ilmenite intergrowths that exceed 100  $\mu\text{m}$  can be found through  
 199 microscopy and <20  $\mu\text{m}$  Fe-Ti oxide grains can be detected with scanning electron mi-  
 200 croscopy (Fig. 2). Based on textural differences Morrison et al. (1983) divided the anorthosite  
 201 xenoliths into four groups: one group which typically have well-developed granoblastic  
 202 texture characterized by equigranular plagioclase crystals; another group which have in-  
 203 terlocking, lath-shaped plagioclase crystals; an intermediate group which can have both  
 204 granoblastic texture and interlocking plagioclase laths; and a brecciated group that have  
 205 brittle deformation textures superposed on pre-existing textures.

## 206 2.2 Portage Lake Volcanics and the Greenstone Flow

207 The Portage Lake Volcanics (PLV) is a ~5 km thick, normally magnetized, dom-  
 208 inantly olivine basalt to andesite volcanic succession that outcrops in northern Michi-  
 209 gan (particularly along the Keweenaw Peninsula) as well as on Isle Royale (Fig. 1, Huber  
 210 (1973); Cannon and Nicholson (2001); Green (1982)). The Greenstone Flow of the Portage  
 211 Lake Volcanic Group has been recognized as one of the largest lava flows on earth (Figs.  
 212 1, 3). It outcrops as the main ridge along the Keweenaw Peninsula and Isle Royale (Fig.  
 213 1). The flow can be correlated between the two outcrop regions on the basis of geochem-  
 214 ical, petrographic, and paleomagnetic similarity of the flow itself and the flows above and  
 215 below (Longo, 1984). In both outcrop regions, the Greenstone Flow is underlain by con-  
 216 glomerate and overlain by pyroclastic breccia (Lane, 1911; Huber, 1973). On the Keweenaw  
 217 Peninsula, the Greenstone Flow is exposed over 90 km with a range of thickness from  
 218 ~100 meters to a maximum thickness of over 450 meters, dipping to the northwest (Fig.  
 219 1; White (1960)). On Isle Royale, the Greenstone Flow has a range of thickness from ~30  
 220 meters to a maximum thickness of about 250 meters, dipping toward the southeast (Fig.  
 221 1; Huber (1973)). More recently, Doyle (2016) estimated that the total aerial extent of

the Greenstone Flow could be up to  $\sim$ 20000 km<sup>2</sup>. Taking a range for this thickness of 100 to 300 meters, Doyle (2016) estimated a total volume of 2000 to 6000 km<sup>3</sup>. This volume range makes the Greenstone Flow one of the largest, if not the largest, single mafic lava flows on Earth (Fig. 3).

According to mineralogical and textural attributes, Doyle (2016) divided the Greenstone Flow into four zones from bottom to top — lower ophitic zone, heterolithic zone, upper ophitic zone, and an amygdaloidal zone. Field observations, geochemical analyses and parent magma calculations conducted by Doyle (2016) suggest that the zoned Greenstone Flow formed through an open-system differentiation of a composite parent magma which is more evolved than the primitive olivine tholeiites generated by the Mid-continent Rift plume. That study proposed that the emplacement of the Greenstone Flow started with a voluminous eruption of olivine tholeiitic magma, forming the ophitic zones which subsequently inflated due to composite intrusions of more evolved basaltic magma which composes the heterolithic zone. A final stage of localized melt migration and differentiation resulted in the heterogeneous composition of the heterolithic zone. A  $^{206}\text{Pb}/^{238}\text{U}$  zircon date of  $1091.59 \pm 0.27$  Ma for the Greenstone Flow was developed from a pegmatoid sample from the heterolithic zone (Swanson-Hysell et al., 2019).

### 3 Methods and Results

#### 3.1 Zircon Geochronology and Geochemistry

A sample of an anorthosite xenolith within the Beaver River diabase was collected for U-Pb geochronology along Hwy 61 across from the Silver Bay taconite plant (MS99033; 91.26358°W 47.28888°N; Fig. 1). This sample comes from the same xenolith sampled for paleomagnetic study as site AX16 which has an exposed diameter of 27.5 meters (Fig. 2). Thin sections were made from the geochronology sample as well as multiple paleomagnetic cores. As is shown in Fig. 2F, plagioclase in this anorthosite xenolith have both equigranular crystals displaying a granoblastic texture and lath-shaped crystals displaying an interlocking texture. The occurrence of both textures is consistent with an interpretation that this anorthosite xenolith formed under elevated temperatures and experienced heating after initial crystallization.

Zircons were separated from a kilogram of the anorthosite using common mineral separation methods (Supporting Information). The separated zircons were subhedral to

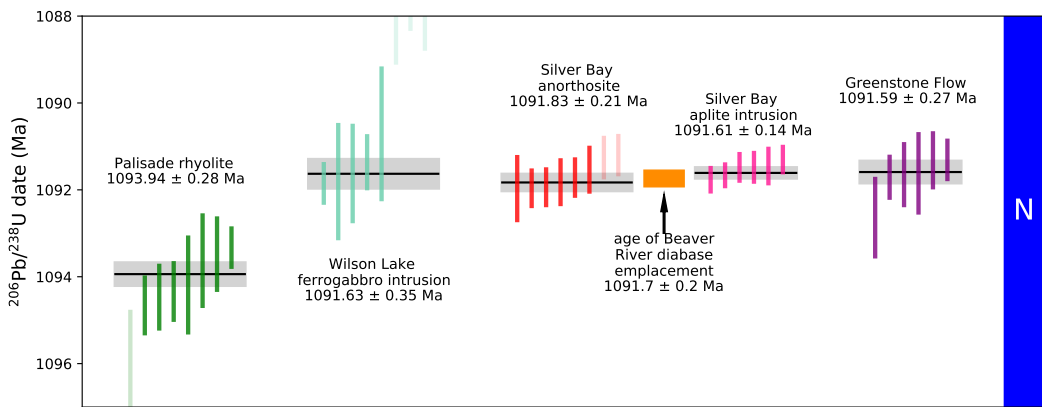


Figure 4: New  $^{206}\text{Pb}/^{238}\text{U}$  zircon date of the anorthosite xenolith (dark orange) plotted in context of previously published  $^{206}\text{Pb}/^{238}\text{U}$  zircon dates from the North Shore Volcanic Group (NSVG) and other Beaver Bay Complex intrusions (Swanson-Hysell et al., 2019, 2020). These high-precision dates are consistent with field observations that the Beaver River diabase crosscuts the Palisade rhyolite (dark green) and is cut by the Silver Bay intrusions (pink). The estimated age of the Beaver River diabase from these constraints is shown with an orange box the represented the 95% confidence interval. Each vertical bar corresponds to one  $^{206}\text{Pb}/^{238}\text{U}$  date from a single zircon crystal. The translucent bars represents zircons with interpreted Pb loss and are therefore not included in the weighted mean age calculations. Horizontal lines and gray boxes represent weighted mean  $^{206}\text{Pb}/^{238}\text{U}$  dates and their analytical uncertainty. The numbers of each geochronology sample corresponds to those in Fig. 1 where locations of these samples are shown.

253 anhedral crystals (z1-z4) and platy fragments (z5-z8). The subhedral to anhedral crys-  
 254 tals are consistent with intercumulus crystallization within an adcumulate with platy frag-  
 255 ments also being a common zircon morphology within anorthosites (e.g. sample AS3 of  
 256 the Duluth Complex anorthositic series; Schmitz et al. (2003)). Eight chemically-abraded  
 257 zircons were analyzed by isotope dilution-thermal ionization mass spectrometry (ID-TIMS)  
 258 in the Boise State Isotope Geology Laboratory using EARTHTIME tracer solutions (Condon  
 259 et al., 2015). Both zircon morphologies yield indistinguishable dates. Using six of these  
 260 single grain dates (and excluding two due to interpreted Pb-loss) results in a weighted  
 261 mean  $^{206}\text{Pb}/^{238}\text{U}$  date of  $1091.83 \pm 0.21/0.37/1.15$  Ma (analytical/ analytical+tracer/  
 262 analytical+tracer+decay uncertainty; Fig. 4).

263 This date provides a tight constraint on the age of the Beaver River diabase. Pre-  
 264 viously, the maximum age constraint for the Beaver River diabase came from the rela-

tionship that it cross-cuts the Palisade rhyolite of the North Shore Volcanic Group which has a  $^{206}\text{Pb}/^{238}\text{U}$  date of  $1093.94 \pm 0.28$  Ma (Swanson-Hysell et al., 2019). With this new date, we know the crystallization age of the diabase to have been near-synchronous or younger than the date from the anorthositic xenolith. The Silver Bay intrusions, from which an aplite has a  $^{206}\text{Pb}/^{238}\text{U}$  date of  $1091.61 \pm 0.14$  Ma, (Fairchild et al., 2017), cross-cut the Beaver River diabase. These dates constrain the diabase to have been emplaced between  $1091.83 \pm 0.21$  and  $1091.61 \pm 0.14$  Ma (Fig. 4). Assuming a uniform probability of diabase emplacement between the anorthositic and aplite dates and their normal distributed uncertainties, a 95% confidence interval on the age of the diabase can be estimated by a Monte Carlo simulation (Supporting Information). This analysis gives an age for the diabase of  $1091.7 \pm 0.2$  Ma (95% CI).

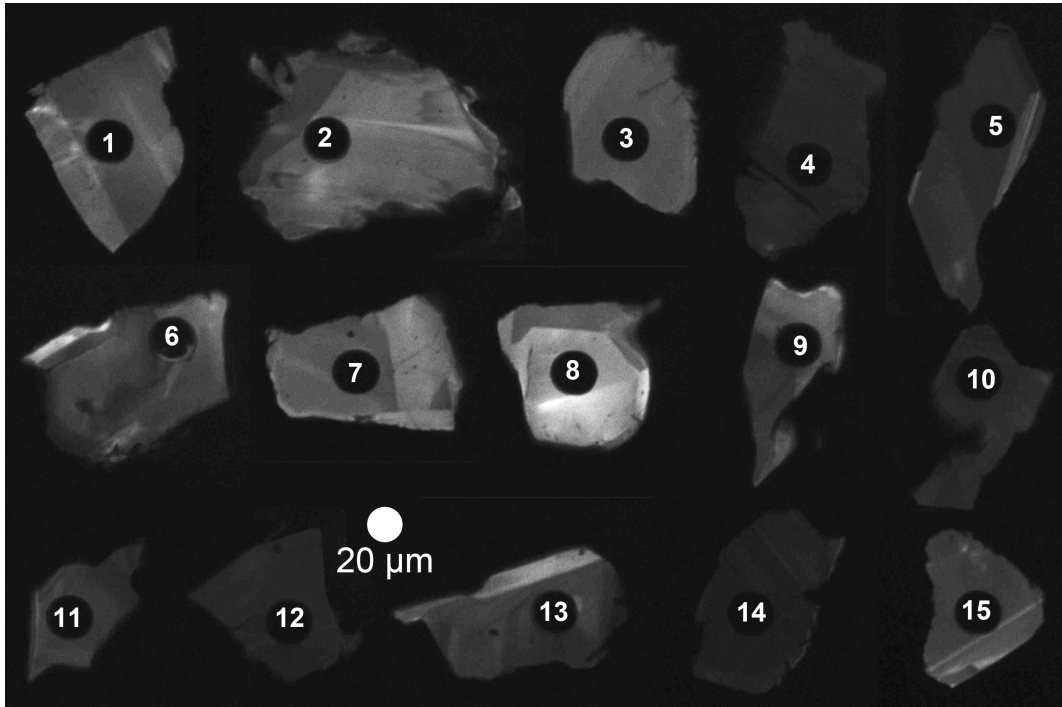


Figure 5: Cathodoluminescence (CL) image montage of the 15 zircons laser-ablated for trace element analysis from sample MS99033. There are sharp boundaries between zones of differing CL response within many of the zircons attributable to variable REE concentrations. For example, the bright zoning in grain 15 has a thickness of  $\sim 2 \mu\text{m}$ . Note that grain 1 (corresponding to spot 1) has a platy morphology, while the rest are subhedral to anhedral.

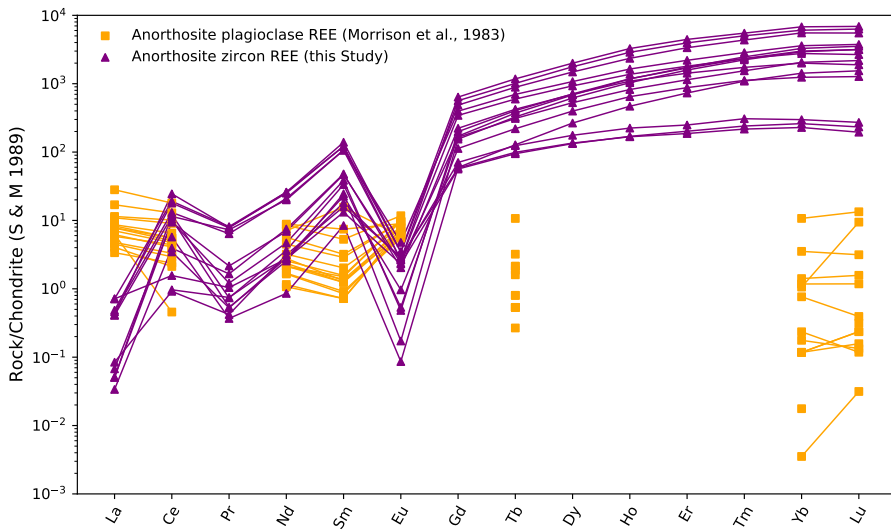


Figure 6: Rare earth element (REE) analyses plagioclase crystals from anorthosite xenoliths (from Morrison et al. (1983)) and from 15 zircons from geochronology sample MS99033 (anorthosite xenolith site AX16) developed by inductively coupled plasma mass spectrometry. All data are chondrite-normalized (Sun & McDonough, 1989).

An additional 15 zircons were characterized using cathodoluminescence (CL) imaging and laser ablation-inductively coupled plasma mass spectrometry (LA-ICPMS), with methods and instrumentation described in the Supporting Information. CL images reveal internal planar zones of variable brightness, often with darker interior zones and outer brighter zones (Fig. 5). All crystals exhibit sharp, micron-scale transitions between zones, and LA-ICPMS analyses quantify CL brightness as correlated with rare earth elements (REE) content. REE patterns in zircons exhibit a significant Chondrite-normalized negative Eu anomaly (Fig. 6). The Ti-in-zircon thermometer gives a range of estimated zircon crystallization temperatures from 998°C to 860°C with a mean of ~950°C (Ferry and Watson (2007); Supporting Information). Decreasing temperatures are correlated with deepening of the negative Eu anomaly and increasing incompatible trace element (e.g. Hf, Th) incorporation into zircon. These data are consistent with a model of magmatic zircon crystallizing from the cooling and fractionating interstitial residual melt within the cumulate plagioclase framework.

290        **3.2 Paleomagnetism**

291        We sampled standard paleomagnetic cores along the southern and eastern Beaver  
 292        Bay Complex with a particular focus on acquiring paired sites of anorthosite xenoliths  
 293        and their local diabase hosts. Sample cores were collected using a hand-held gasoline-  
 294        powered drill and were oriented using a magnetic compass as well as a sun compass when  
 295        possible. Sun compass orientations were preferentially used for determining the sample  
 296        azimuth. Typically, 7-10 cores were drilled for each anorthosite xenolith and their dia-  
 297        base hosts. A total of 17 diabase and 22 anorthosite sites were collected (Table 1). A  
 298        table that summarizes the measured dimensions of each anorthosite xenolith sampled  
 299        and the distance between each anorthosite paleomagnetic site and closest diabase host  
 300        site is provided in the Supporting Information.

301        Samples underwent step-wise demagnetization and analyses in the magnetically shielded  
 302        room in the UC Berkeley Paleomagnetism Lab. 7 sites from the Beaver River diabase  
 303        underwent alternating field (AF) demagnetization with peak fields from 1 mT to 130 mT.  
 304        An ASC TD-48SC thermal demagnetizer was used to demagnetize 10 diabase sites and  
 305        all 22 anorthosite sites in a step-wise manner, with reduced step increments between 540°C  
 306        and 585°C. The typical magnetic field inside the shielded room is <500 nT and the field  
 307        inside the thermal demagnetizer chamber is <10 nT. The quartz glass sample rod of the  
 308        UC Berkeley system is typically measured at  $5 \times 10^{-12}$  Am<sup>2</sup>. All remanence measure-  
 309        ments were made on a 2G Enterprises DC-SQUID superconducting rock magnetometer  
 310        equipped with inline AF coils and an automated sample changer system. The PmagPy  
 311        software package was used to implement least-square fits to specimen demagnetization  
 312        data (Tauxe et al., 2016). Measurement level data are available within the MagIC database  
*for the purposes of review, these data are available in a pre-publication contribution within*  
 313        *the MagIC database that can be accessed here: <https://earthref.org/MagIC/17102/400e0fb3-a79b-42bd-aeab-9005d2e3b438>*  
 314        *400e0fb3-a79b-42bd-aeab-9005d2e3b438*

316        For both the diabase and anorthosite demagnetization, principal component anal-  
 317        yses show that an origin trending characteristic remanent magnetization (ChRM) can  
 318        be isolated after the removal of a minimal secondary component during the first few low  
 319        coercivity (<10 mT) or low temperature (<200°C) demagnetization steps (Fig. 7). The  
 320        ChRMs typically unblock through thermal demagnetization steps from ~500°C to ~580°C,  
 321        consistent with them being held by low-titanium titanomagnetite. We interpret this com-

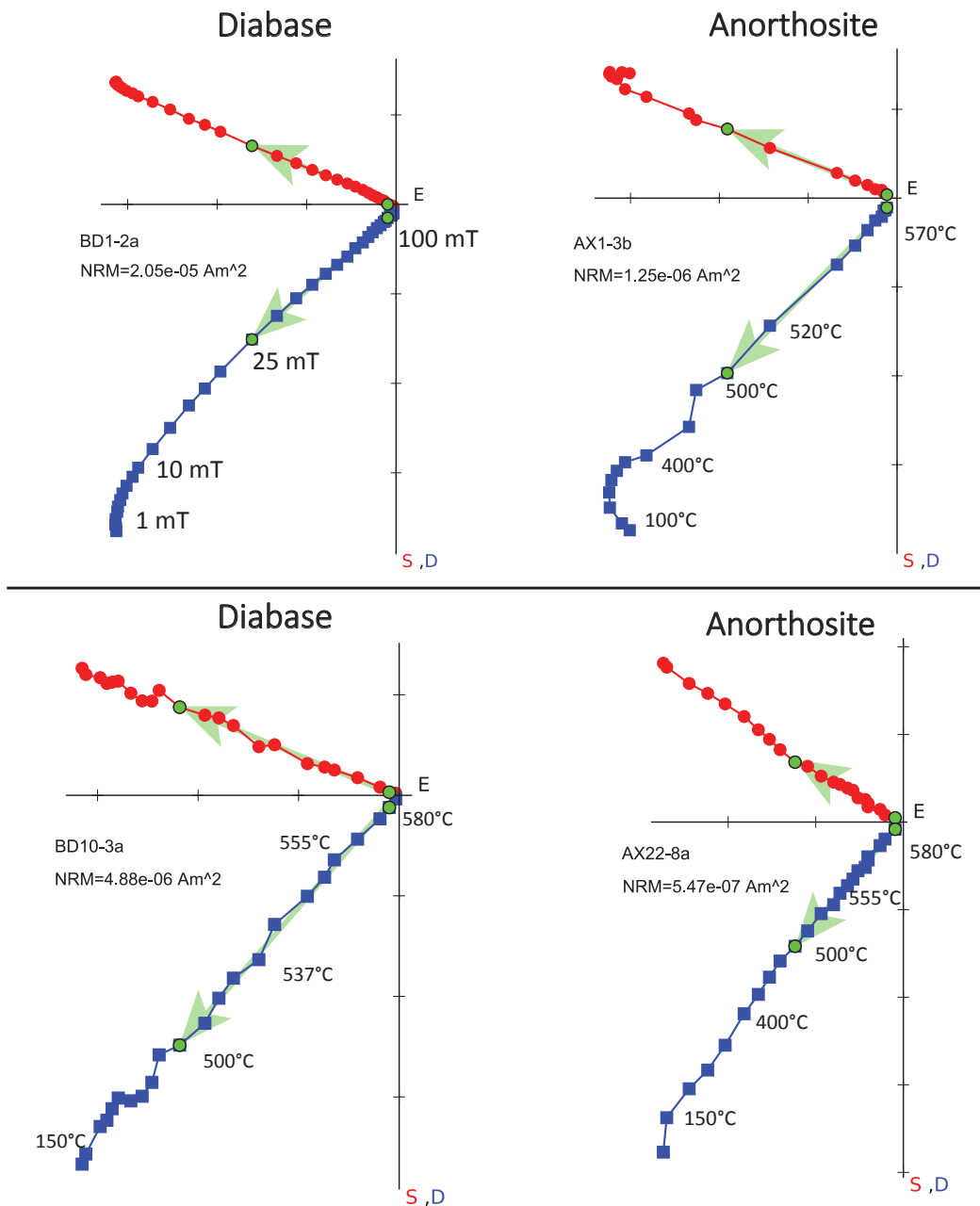


Figure 7: Example orthogonal vector demagnetization diagrams for diabase and anorthosite specimens. Anorthosite site AX1 is from a xenolith within the diabase sampled as BD1. Similarly, AX22 is from a xenolith with the BD10 diabase. Both AF and thermal demagnetization show dominantly univectoral decay of characteristic remanent magnetizations (ChRM) toward the origin after removal of minimal secondary components. The data reveal very similar ChRM directions between the paired diabase and anorthosite xenoliths sites.

322 ponent as a primary remanent magnetization acquired during the emplacement and cool-  
 323 ing of the Beaver River diabase.

324 The site mean paleomagnetic directions are shown in Table 1. We present both AF  
 325 and thermal demagnetization results for the Beaver River diabase as both methods are  
 326 effective in removing the secondary components and isolating the coherent and univec-  
 327 toral ChRM. Based on specimen and site level demagnetization behavior and the prox-  
 328 imity between paired paleomagnetic sites of the anorthosite xenoliths and the diabase,  
 329 we grouped the anorthosite xenoliths and their diabase hosts into individual cooling units  
 330 and calculated a paleomagnetic pole position as the mean of the cooling unit virtual ge-  
 331 omagnetic poles (Fig. 8).

332 Tilt-correcting the paleomagnetic directions to paleohorizontal is necessary for de-  
 333 veloping accurate paleomagnetic poles from the diabase and the anorthosite xenoliths  
 334 to be compared to the Keweenawan Track apparent polar wander path (APWP; Fig. 8,  
 335 Swanson-Hysell et al. (2019)). For intrusive igneous rocks, tilt corrections can be diffi-  
 336 cult to constrain due to the lack of a clear paleohorizontal reference. Many paleomag-  
 337 netic studies of Midcontinent Rift intrusive rocks in the Lake Superior region did not ap-  
 338 ply tilt corrections to their data (e.g., Beck & Lindsley, 1969; Beck, 1970; Books et al.,  
 339 1966). However, we can determine the structural orientation of the Beaver River diabase  
 340 using the abundant igneous fabric orientations measured on the diabase as well as bed-  
 341 ding orientations measured from adjacent volcanic units (Boerboom, 2004; Boerboom  
 342 & Green, 2006; Boerboom et al., 2006, 2007; Miller et al., 2001). We compile the igneous  
 343 layering measurements from the Beaver River diabase and the volcanic bedding ori-  
 344 entations from the Schroeder-Lutsen basalt which is overlying the Beaver Bay Complex.  
 345 The mean tilt orientations of both units are similar (diabase dip direction - dip: 128.5  
 346 - 10.2; basalt dip direction - dip: 142.2 - 13.6). We combine the structural measurements  
 347 from the Beaver River diabase and the Schroeder-Lutsen basalt and derived two sets of  
 348 tilt corrections for the paleomagnetic directions of the diabase and anorthosite (dip di-  
 349 rection - dip in the southern Beaver Bay complex: 128.7 - 12.9; in the eastern Beaver Bay  
 350 Complex: 145.6-13.1, Supporting Information). The advantage of using the structural  
 351 orientations from the Schroeder-Lutsen basalt is that the arcuate shape of the Beaver  
 352 River diabase intrusions is nicely captured by the variation of lava dip directions while  
 353 the dip angles of the basalt and diabase are very similar (Fig. 1).

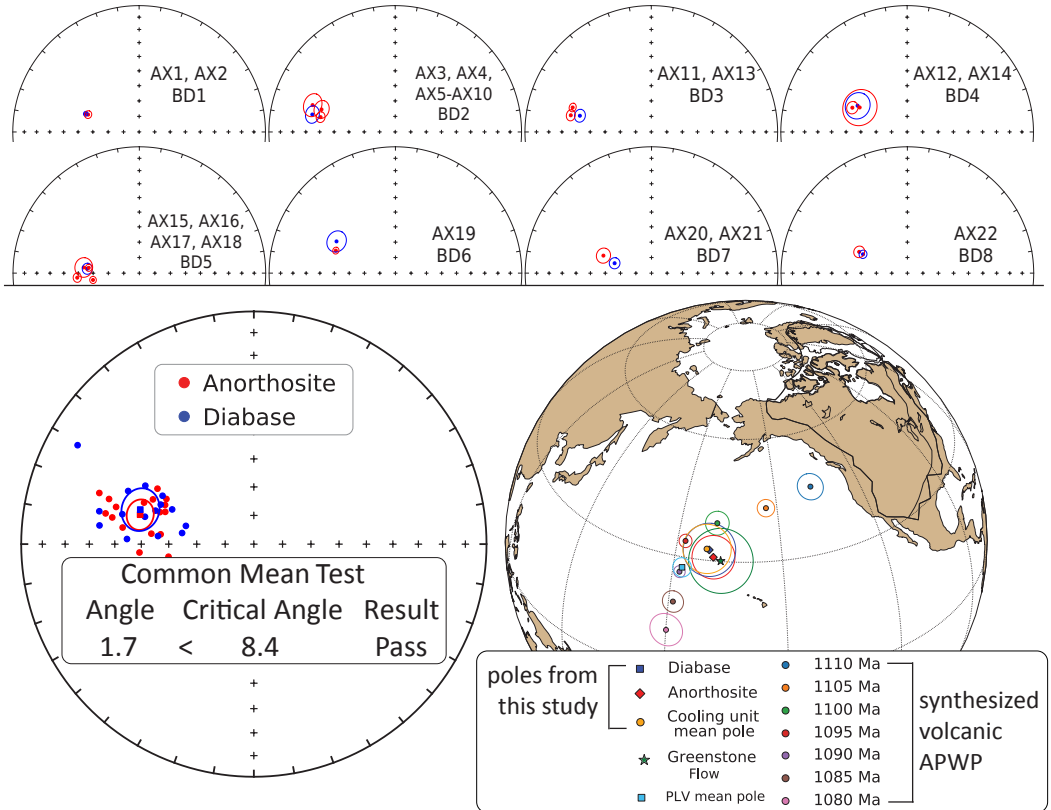


Figure 8: Top: Equal area plots of paleomagnetic directions from the anorthosite xenoliths and their local diabase hosts. AX: anorthosite xenolith site; BD: Beaver River diabase site. Bottom: Site mean paleomagnetic directions from the Beaver River diabase and anorthosite xenoliths are plotted on equal area plots. The anorthosite and diabase sites share a common mean as summarized by the results of the McFadden and McElhinny (1990) common mean test. Mean paleomagnetic pole positions of all diabase sites, all anorthosite sites, as well as a grand mean pole developed by grouping the anorthosite and diabase sites into individual cooling units are plotted against a synthesized Laurentia APWP based on poles from Midcontinent Rift volcanics and sedimentary rocks (Swanson-Hysell et al., 2019). The paleomagnetic poles from the diabase and anorthosite are indistinguishable with the Greenstone Flow pole developed by Foucher (2018), but they all are distinct from the Portage Lake Volcanics mean pole (Swanson-Hysell et al., 2019). All directions shown are tilt corrected.

The tilt-corrected ChRM<sub>s</sub> in both lithologies are northwest and down, yielding good specimen-level and site-level consistency (Fig. 7, 8). Close directional similarities between each anorthosite xenolith and their host diabase are supported by 9 out of a total of 17 diabase-anorthosite paleomagnetic site pairs passing a common mean test (McFadden & McElhinny, 1990). The overall mean directions between the two lithologies are indistinguishable as they also pass a common mean test (Fig. 8, McFadden and McElhinny (1990)). For the anorthosite sites that do not pass a common mean test with their diabase hosts, they nevertheless have coherent specimen-level directions that are close to their host diabase directions (Fig. 8). We also plot the tilt-corrected mean pole of sites from both lithologies (diabase: 32.5°N, 189.5°E, N = 15, A95 = 6.3, k = 37.4; anorthosite: 30.9°N, 190.8°E, N = 17, A95: 5.2, k = 48.5) in context of a previously synthesized APWP from the volcanics of the Midcontinent Rift (Swanson-Hysell et al., 2019) and show the poles to lie near the expected 1090 Ma and 1095 Ma pole positions (Fig. 8). The mean pole position of the interpreted cooling units (32.7°N, 188.8°E, N = 15, A95 = 5.9, k = 41) lies close to the mean pole position derived from the *ca.* 1092 Ma Portage Lake Volcanics (Fig. 8), consistent with the coeval magmatic activity between the Beaver River diabase and the Portage Lake Volcanics. This cooling unit mean pole paired with the estimated diabase emplacement age of 1091.7 ± 0.2 Ma is recommended to be used to as a paleomagnetic pole for the Beaver River diabase in future Laurentia Midcontinent Rift APWP compilations.

### 3.3 Thermal history model

The consistency of the paleomagnetic directions between the anorthosite xenoliths and the host diabase indicate that the anorthosites were heated above the Curie temperature of low-titanium titanomagnetite (~580°C) within the Beaver River diabase. To determine whether this thermal history is consistent with the geometry of the units and to gain more insight into the emplacement history of the xenoliths, we developed a cooling model. In this model, the anorthosite xenoliths are considered to be solid spheres with an initial cool temperature embedded in a uniform sheet of diabase magma (Delaney, 1987; Unsworth & Duarte, 1979). The modeled thermal histories for various sizes of anorthosite xenoliths are shown in Fig. 9. In one end member case, the initial temperature of the anorthosites is assumed to be 50°C. While this temperature is unrealistically low given that the anorthosites likely have a deep crustal source, thermal modeling shows that even

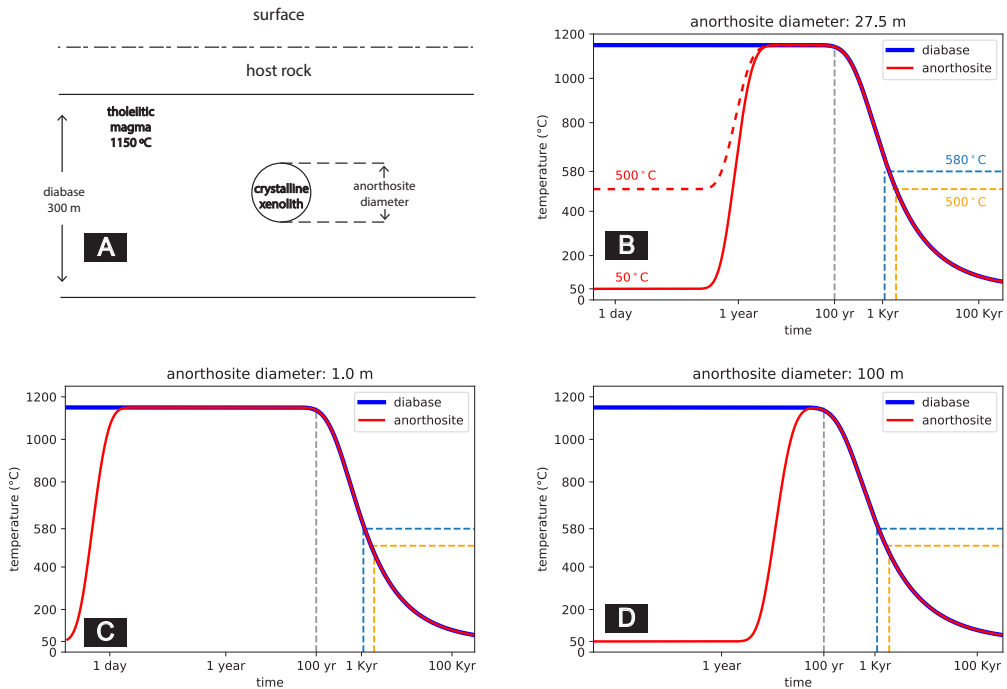


Figure 9: Thermal history model of the Beaver River diabase and its anorthosite xenoliths after emplacement at hypabyssal depths. (A) Schematic diagram for the thermal model considering cool anorthosite xenoliths as crystalline spheres residing in the middle of a diabase sill. Together they are hosted by cool country rocks at shallow depths. (B) Specific model for anorthosite AX16 (diameter of 27.5 meters) within its diabase sill host which is estimated to be 323 meters thick. (C) Thermal history model considering an anorthosite xenolith 1 meter in diameter residing in a 300 meter diabase sill. (D) Thermal history model considering an anorthosite xenolith 100 meter in diameter residing in a 300 meter diabase sill. These models show that anorthosite xenoliths were heated up to the diabase melt temperature after the emplacement, regardless of size. The time elapsed between magnetite blocking temperatures (580°C and 500°C) during cooling is on the scale of a thousand years.

a 100-meter anorthosite xenolith with such low initial temperature would have been heated to the temperature of the tholeiitic magma ( $1150^{\circ}\text{C}$ ) within the sill. This temperature is well above the Curie temperature of magnetite. Anorthosite xenoliths with an assumed initial temperature of  $500^{\circ}\text{C}$  will equilibrate with the magma temperature on a similar, but slightly shorter, timescale. Therefore, the model predicts that the remanent magnetizations of the anorthosites will be reset during emplacement within the diabase sills, regardless of their initial temperatures. Model parameters set to match the xenolith AX16, from which a U-Pb date was developed in this study, leads to a model where the 27.5 m xenolith would have stayed at the magma temperature for about 100 years after sill emplacement (Fig. 9). This duration estimate is a minimum as it does not consider heating associated with melt in the lower crust or during ascent prior to emplacement although this was likely rapid. The xenolith would have then cooled through the Curie temperature of magnetite ( $580^{\circ}$ ) after  $\sim 1$  kyr and acquired its magnetization as it cooled through magnetite blocking temperatures (down to  $\sim 500^{\circ}$ ).

## 4 Discussion

### 4.1 Origin and Age of the Anorthosite Xenoliths

There have been divergent interpretations regarding the age and magma source of the anorthosite xenoliths in the Beaver River diabase (Fig. 1). Grout (1939) recognized the xenolithic nature of the anorthosites and suggested that the massive intrusion of the older anorthositic gabbro within the Duluth Complex may have supplied anorthosite fragments that were later entrained by the Beaver River diabase emplacement. Morrison et al. (1983), on the other hand, argued that the xenoliths were sourced from Paleoproterozoic or Archean lower crust that were liberated and contaminated by Midcontinent Rift magmas based on Sm and Nd isotopic data. They interpreted a Sm-Nd model age of 1.9 Ga from one of the xenoliths as providing a minimum crystallization age for the anorthosites though they acknowledged that these constraints are not definitive with respect to the age.

In contrast to this Archean to Paleoproterozoic model, Miller and Chandler (1997) favored a scenario where the anorthosite crystallized as part of Midcontinent Rift magmatism. They cited work by Kushiro (1980) who showed that the changing density contrast between labradoritic to bytownitic plagioclase and tholeiitic magma at different crustal

417 pressures would promote flotation of plagioclase in deep (>20 km) crustal magma cham-  
 418 bers and the creation of anorthosite cumulates in the lower crust. This mechanism of  
 419 plagioclase flotation likely created massive anorthosite cumulates in the roof zones of sub-  
 420 crustal magma chambers during MCR magmatism. Miller and Weiblen (1990) specu-  
 421 lated that plagioclase-phyric magmas tapped from these deep chambers fed shallow (~5km)  
 422 subvolcanic intrusions of the Duluth Complex, thereby creating the anorthositic gabbros  
 423 of the Anorthositic Series. Miller and Chandler (1997) suggested that the nearly pure  
 424 anorthosite xenoliths occurring in the younger and more hypabyssal diabase intrusions  
 425 of the Beaver Bay Complex were harvested from these phase-segregated intrusions in the  
 426 lower crust. They further argued that the isotopic data of Morrison et al. (1983) can be  
 427 explained by anorthosite-forming MCR magmas having been contaminated by older crust  
 428 rather than the anorthosites being older lower crust that was contaminated by MCR mag-  
 429 mas.

430 Our new geochronology documents that the anorthosite xenoliths were liberated  
 431 from depth and emplaced within the shallow intrusions of the Beaver River diabase at  
 432  $1091.7 \pm 0.2$  Ma (95% CI). This timing of emplacement is constrained by the Beaver River  
 433 diabase postdating the new  $^{206}\text{Pb}/^{238}\text{U}$  zircon date of  $1091.83 \pm 0.21$  Ma for the AX16  
 434 xenolith and being older than the cross-cutting  $1091.61 \pm 0.14$  Ma Silver Bay intrusives.

435 The most straight-forward interpretation of the anorthosite  $1091.83 \pm 0.21$  Ma U-  
 436 Pb zircon dates is that they record crystallization of the anorthosite cumulates during  
 437 Beaver Bay Complex magmatism just before the time of Beaver River diabase emplace-  
 438 ment. The significant negative Eu anomaly in the zircons within the anorthosite con-  
 439 strains them to have crystallized from a magma that had experienced significant plago-  
 440 clase extraction (Fig. 6; Rubatto (2002); Schaltegger et al. (1999)). This result indicates  
 441 that the zircons were comagmatic with their host anorthosite plagioclase. The Ti-in-zircon  
 442 temperature estimates indicate that they crystallized from temperatures of ~998 to 860°C  
 443 (Supporting Information; Ferry and Watson (2007)). In addition, zircons that have lower  
 444 Ti-in-zircon temperatures have lower Eu abundance, but enrichment of incompatible el-  
 445 ements such as Hf and Th (Supporting Information). This systematic pattern of elemen-  
 446 tal concentration variation is consistent with the zircons crystallizing from residual melts  
 447 on a cooling path that increased incorporation of incompatible trace elements and deep-  
 448 ened the Eu anomaly with decreasing temperature and melt fraction. Scanning electron  
 449 microscopy on two undated anorthosite xenoliths with plagioclase laths displaying in-

450 terlocking textures reveals zircon crystals with subhedral to anhedral shapes within the  
 451 mineral assemblage that is interstitial to the plagioclase (Supporting Information). Cathodo-  
 452 luminescence (CL) images show internal zoning in zircons which can be attributed to vari-  
 453 ations in REE, particularly Dy elemental concentrations, during zircon crystallization  
 454 (Fig. 5; Remond et al. (1992)). These data confirm that the zircons formed from resid-  
 455 ual melt within the interstitial spaces of the plagioclase cumulate and are inconsistent  
 456 with a later metamorphic origin.

457 This scenario requires that there were large lower crustal magma chambers in which  
 458 flotation of plagioclase resulted in cumulate formation both during *ca.* 1092 Ma Beaver  
 459 Bay Complex magmatism and contrasts with the model of Miller and Chandler (1997)  
 460 for an older origin in the *ca.* 1096 Ma Duluth Complex magmatism. Zircon U-Pb dates  
 461 nearly always record crystallization age as the temperatures necessary for significant dif-  
 462 fusive Pb loss exceed typical liquidus temperatures of zircon-bearing rocks. However, the  
 463 anorthosites are a rather unique case given that the melting point of anhydrous plagio-  
 464 clase with an average composition of the Beaver River anorthosite (~70% anorthite, Morrison  
 465 et al. (1983); Doyle (2016)) is quite high at ~1400°C. Thermal modeling indicates that  
 466 the xenoliths would have equilibrated to the temperature of the olivine tholeiitic magma  
 467 (~1100 to 1200°C) and remained at that temperature for more than 100 years in the di-  
 468 abase sill interior (Fig. 9). While these temperatures would not have melted the plagio-  
 469 clase or zircon, these temperatures are high enough to consider the possibility of Pb dif-  
 470 fusion out of zircon. Could diffusive resetting of the zircon in the anorthosite cumulates  
 471 xenoliths allow their crystallization at *ca.* 1096 Ma in the deep crust, but the closure of  
 472 U-Pb zircon chronometer upon emplacement and cooling at *ca.* 1091.8 Ma?

473 The magnitude of Pb diffusion is dependent on the time spent at such a temper-  
 474 ature. Using the diffusion parameters of Cherniak and Watson (2001), a sustained tem-  
 475 perature of 1200°C for ~10 thousand years is required for diffusive loss of ~90% of Pb  
 476 from a ~120  $\mu\text{m}$  diameter zircon. In this case, zircons that crystallized at 1096 Ma and  
 477 then lost >90% of their Pb at 1091.6 Ma could give apparent U-Pb dates of 1091.8 Ma  
 478 that are reproducible at the measurement resolution (Supporting Information). How-  
 479 ever, CL imagery reveals sharp boundaries between zones of differing CL response (Fig.  
 480 5) on the scale of ~2  $\mu\text{m}$ . Such CL zoning patterns are dominantly attributed to con-  
 481 centration variations in the rare earth element Dy (Remond et al., 1992). A time-temperature  
 482 history that results in 90% Pb diffusion out of a 120  $\mu\text{m}$  diameter zircon would also cause

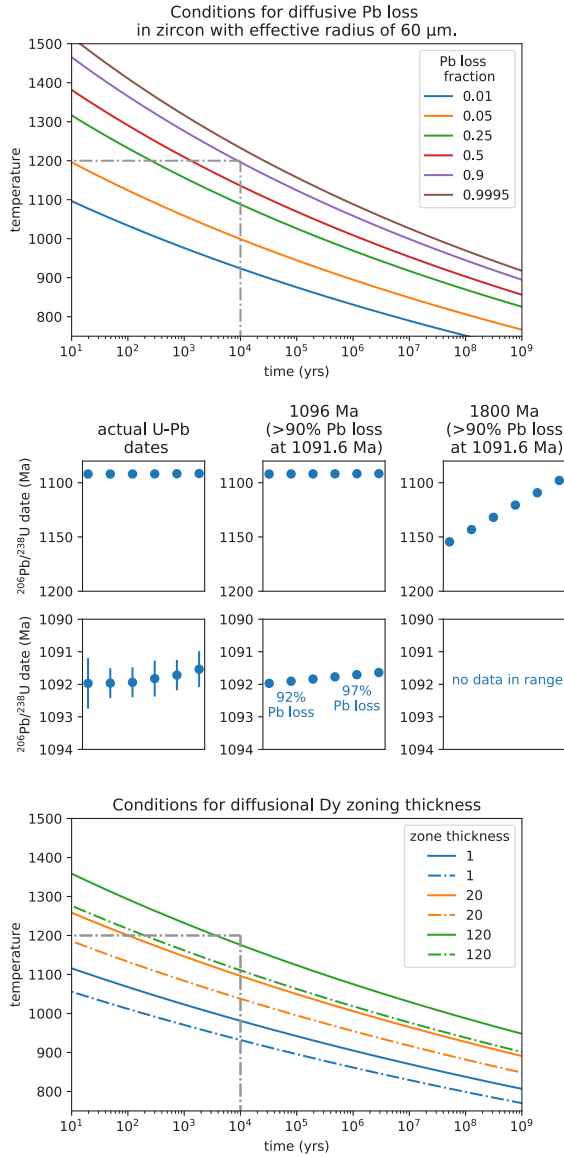


Figure 10: Top: Conditions for diffusive Pb loss in crystalline zircon for zircons of effective radii of 60  $\mu\text{m}$ . Curves represent time–temperature conditions under which zircon will lose the indicated fraction of total Pb; Middle: Modeled zircon Pb loss scenarios with initial crystallization of 1091.8 Ma, 1096 Ma, and 1800 Ma ages with varying degrees of Pb loss at 1091.6 Ma compared to the actual U-Pb dates; Bottom: Preservation of Dy zoning in zircon. Curves represent time-temperature conditions under which different zoning thicknesses would be preserved in zircon. For conditions above the upper solid curves in each group, well-defined zoning will be lost. For conditions above the dashdot lines zones will be partially lost but still retain initial composition in zone center. Pb diffusion and Dy zoning models are replotted from (Cherniak et al., 1997).

483 Dy re-equilibration throughout a zircon, leaving no clear zonation (Fig. 10; Cherniak et  
 484 al. (1997)). Therefore, a scenario where the zircons first crystallized during Duluth Com-  
 485 plex magmatism and subsequently lost more than 90% of Pb is exceedingly difficult to  
 486 reconcile with the preservation of such thin, sharp zones. In fact, preservation of REE  
 487 zoning in these zircons limits heating at the emplacement temperatures of the Beaver  
 488 River diabase to a duration more consistent with our modeled entrainment and cooling  
 489 duration of ~100 years. It is therefore most probable that the Beaver River diabase anorthosite  
 490 xenoliths are entrained cumulate enclaves that formed at the time of Beaver Bay Com-  
 491 plex magmatism.

492 **4.2 A comagmatic relationship between the Beaver River diabase and**  
 493 **the Greenstone Flow**

494 Given the existence of many anorthosite xenoliths whose short-axis diameters of-  
 495 ten reach tens of meters and can be as wide as 180 meters (Fig. 1; Boerboom (2004);  
 496 Boerboom et al. (2006)), the Beaver River diabase magma conduits must have been at  
 497 least this wide during magma ascent. It would be consistent with such wide conduits ex-  
 498 tending to hypabyssal depths for magma that flowed through these conduits to have vented  
 499 to the surface.

500 The high volume and composite nature of the extrusive Greenstone Flow of the Portage  
 501 Lake Volcanics lead to a match for this large and composite feeder system. Doyle (2016)  
 502 proposed a comagmatic link between the Beaver River diabase and the Greenstone Flow.  
 503 Doyle (2016) discovered that both the intrusive Beaver River diabase and the Greenstone  
 504 Flow have indistinguishable primary compositions that followed similar differentiation  
 505 patterns. Doyle (2016) also highlighted the shared petrographic textures between the  
 506 ophitic Beaver River diabase and the ophitic Greenstone Flow, which features the pla-  
 507 gioclase laths clustering together and joining along their long crystallographic axes. The  
 508 fosterite content of the olivines and enstatite content of the pyroxenes in the Beaver River  
 509 diabase together with the Silver Bay intrusions, and the Greenstone Flow have overlap-  
 510 ping compositions consistent with the same magma source (Fig. 11). The composition  
 511 of the plagioclase within the units further strengthens this interpretation. Although there  
 512 are no known multi-crystalline anorthosite xenoliths in the Greenstone Flow, plagioclase  
 513 megacrysts occur in the lava flow. Analyses of the anorthite content from plagioclase megacrysts  
 514 show very similar values between the Beaver River diabase and the Greenstone Flow basalt

(Fig. 11, Doyle (2016)). In both units, the plagioclase cores are more enriched in anorthite than the rim and the groundmass. These data provide evidence that the core of the plagioclase megacrysts in the Greenstone Flow derived from a similar source with those in the Beaver River diabase and that the rims are later overgrowths. These mineralogical similarities are consistent with the interpretation that the Beaver River diabase and the Greenstone Flow have the same magma source.

The magmatic linkage between the Beaver River diabase and the Greenstone Flow inferred from comparable lithologies and geochemistry can be further evaluated using the paleomagnetic pole positions and radioisotopic dates from both units (Fig. 8, 4). The heat diffusion model of the cooling history of the anorthosite xenoliths within the diabase suggests that the time it takes to cool the diabase and anorthosite from low-titanium titanomagnetite Curie temperature ( $\sim 580^{\circ}\text{C}$ ) to their blocking temperatures ( $\sim 500^{\circ}\text{C}$ ) is on the time scale of a few thousand years (Fig. 9). This time scale is close to the typical  $10^4$  years which is considered to be sufficient for averaging out secular variations of the geomagnetic field. Fig. 8 shows the site mean paleomagnetic pole positions from all diabase and anorthosite sites in this study against the previously synthesized Laurentia APWP developed using an Euler pole inversion to chronostratigraphically constrained volcanic poles in present-day coordinates (Swanson-Hysell et al., 2019). The site-mean pole positions of the diabase and anorthosite overlap within uncertainty ellipses and the mean pole positions fall between the 1095 Ma and 1090 Ma pole path positions (Fig. 8), consistent with the geochronology results (Fig. 4). Further, the mean paleomagnetic pole position derived from the Greenstone Flow share a common mean with those of the Beaver River diabase and the anorthosite xenoliths, but none of these poles share a common mean with the mean pole derived from the Portage Lake Volcanics (Fig. 8; Swanson-Hysell et al. (2019)). This result suggests that the timescale over which the Beaver River diabase and the Greenstone Flow acquired their magnetization may be too short to fully average out secular variation. In this case, the overlapping pole positions between the Beaver River diabase and the Greenstone Flow strengthens their temporal correlation even more (Fig. 8).

The U-Pb dates provide strong support for this hypothesis by revealing equivalent ages for the Beaver River diabase and the Greenstone Flow. The age of the Beaver River diabase is constrained to be between the  $^{206}\text{Pb}/^{238}\text{U}$  dates of  $1091.83 \pm 0.21$  Ma and  $1091.61 \pm 0.14$  Ma (Fig. 4) giving an age estimate of  $1091.7 \pm 0.2$  Ma (95% CI). This age is in-

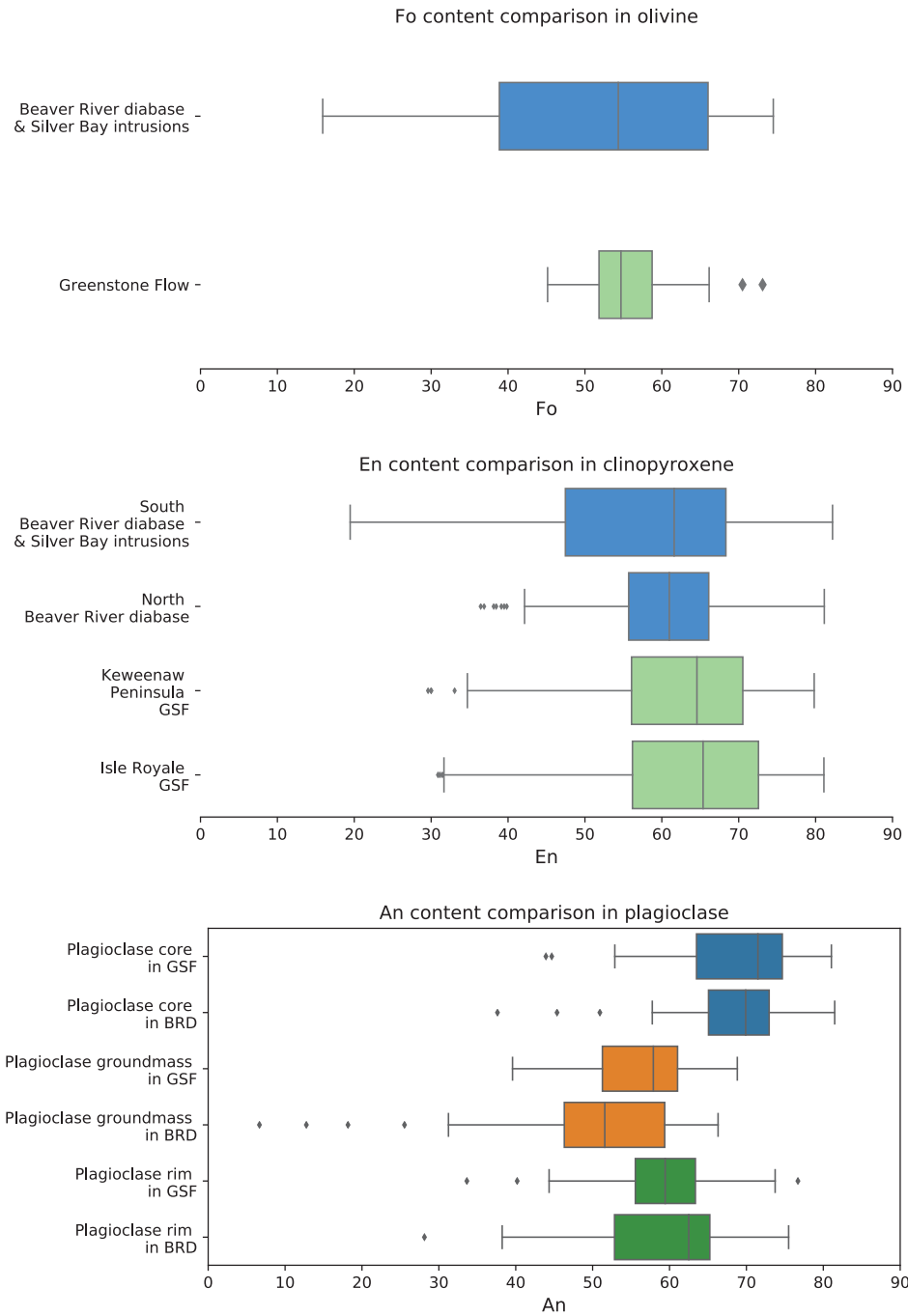


Figure 11: Box plots of geochemical analyses of olivine, pyroxene, and plagioclase in the Beaver River diabase (BRD) and Greenstone Flow (GSF). The fosterite content in olivine crystals and the enstatite content in clinopyroxene crystals are very similar in the Beaver River diabase and the Greenstone Flow. The anorthite concentrations in the core, groundmass, and rim of the plagioclase megacrysts within the Beaver River diabase and the Greenstone Flow share very similar patterns and the distributions are nearly identical. The box encloses the middle 50% of the data ranges (i.e., the interquartile range), and the notch represents the median values. The whiskers extend to the 2.5th and 97.5th percentile values. Fo-fosterite; En-enstatite; An-anorthite. Data from Doyle (2016).

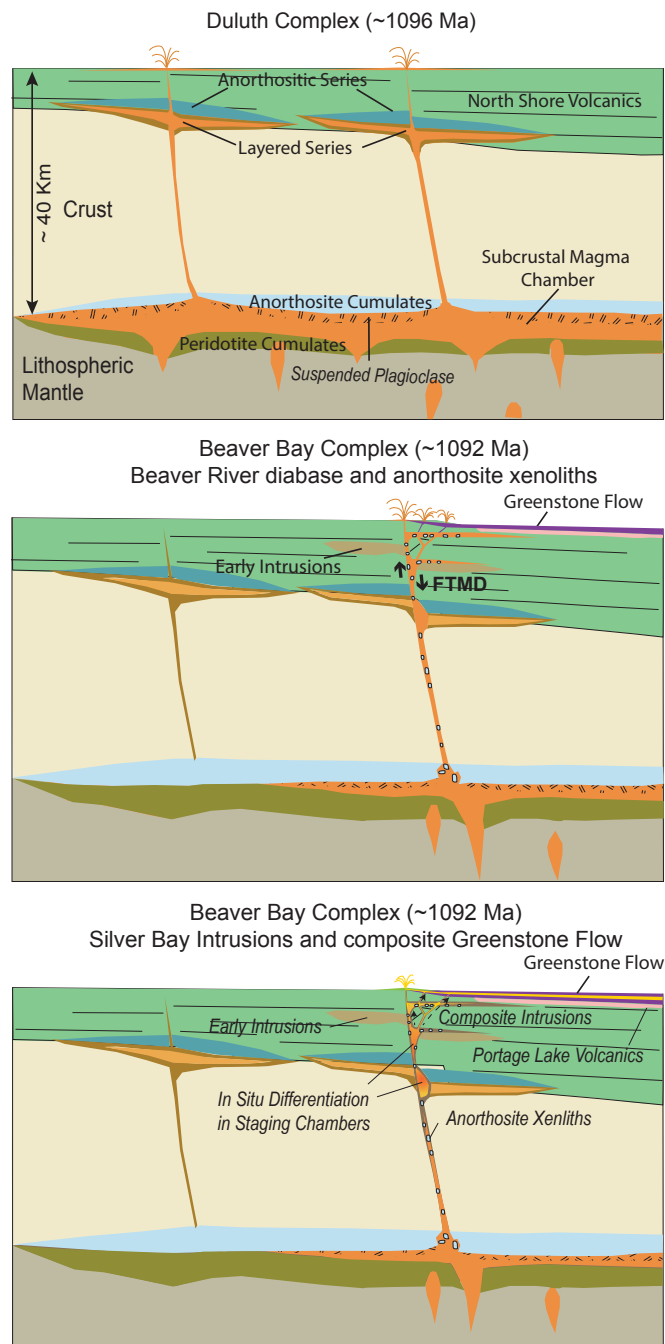


Figure 12: Schematic model for the emplacement of the *ca.* 1096 Ma Duluth Complex, the *ca.* 1092 Ma Beaver Bay Complex, Greenstone Flow and associated anorthositic lithologies. Top: Duluth Complex Anorthositic Series formed by subhorizontal emplacement of plagioclase crystal mushes generated by plagioclase flotation in subcrustal magma chambers. The Layered Series formed by emplacement of crystal-poor mafic magmas beneath the Anorthositic Series and variable differentiation by in situ fractional crystallization. Middle: Intrusion of the anorthosite xenolith-bearing Beaver River diabase of the Beaver Bay Complex along a major crustal fault (FTMD-Finland Tectonomagnetic Discontinuity) and its massive eruption at surface to form the Greenstone Flow. Bottom: Emplacement of the composite Beaver River diabase and Silver Bay intrusions into the diabase and the Greenstone Flow were generated by differentiation in deeper staging chambers. The erosional unconformity between the Schroeder-Lutsen basalt and the Beaver River diabase suggest the diabase was emplaced into an uplifted rift flank highland, allowing for flank eruptions of the Greenstone Flow into the main Midcontinent Rift basin.

548 distinguishable with the  $^{206}\text{Pb}/^{238}\text{U}$  date of  $1091.59 \pm 0.27$  Ma for the Greenstone Flow  
 549 (Fig. 4). These chronological constraints are consistent with a comagmatic linkage be-  
 550 tween the Beaver River diabase and the Silver Bay intrusions and the extrusive Green-  
 551 stone Flow.

552 The Portage Lake Volcanics, including the Greenstone Flow, are interpreted to have  
 553 erupted into the main central graben of the Midcontinent Rift during an interval of sig-  
 554 nificant subsidence (Fig. 12; Miller and Chandler (1997); Cannon and Hinze (1992)). In  
 555 contrast to the thick accumulation in the Portage Lake Volcanics, the Beaver Bay Com-  
 556 plex has an erosional (and slightly angular) unconformity atop it that is then covered  
 557 by the younger Schroeder-Lutsen basalt (Fig. 1; Miller et al. (2001)). This relationship  
 558 suggests that the Beaver River diabase was emplaced into a rift flank highland that ex-  
 559 perienced uplift during the active development of the central graben (Swanson-Hysell  
 560 et al., 2019). Eruptions fed through the Beaver River diabase network could have emerged  
 561 from the rift flank or flowed from the highland into main rift basin where it accumulated  
 562 as the Greenstone Flow and associated Portage Lake Volcanics (Fig. 12). Silver Bay in-  
 563 trusions from chambers of differentiated staging magmas later intruded the Beaver River  
 564 diabase and the Greenstone Flow, adding to the composite lithologies of the lava flow  
 565 and further inflating its heterolithic zone (Fig. 12). If the Greenstone Flow indeed con-  
 566 nects through the Lake Superior basin to NE Minnesota and the Beaver River diabase,  
 567 the volume of  $\sim 1650 \text{ km}^3$  estimated by Longo (1984) must be a minimum. The full vol-  
 568 ume of the Greenstone Flow likely reaches  $\sim 6000 \text{ km}^3$  (Doyle, 2016), rivaling the largest  
 569 known lava flows on Earth (Fig. 3).

## 570 5 Conclusion

571 High-precision U-Pb dates, together with paleomagnetic data, support the hypoth-  
 572 esis that the Beaver River diabase was a feeder system to the high-volume Greenstone  
 573 Flow. This intrusive-extrusive linkage is further bolstered by the similar compositions  
 574 of the units. The large anorthosite xenoliths within the Beaver River diabase require that  
 575 conduits feeding the magma to the surface had widths that exceeded 150 meters. As a  
 576 result, there was voluminous emplacement of magma into the shallow subsurface and erup-  
 577 tion into the Midcontinent Rift basin *ca.* 1092.7 Ma at the end of the main stage of Mid-  
 578 continent Rift magmatism.

579 **Acknowledgments**

580 Project research was supported by NSF CAREER grant EAR-1847277 to N.L.S.-H. and  
581 an Institute on Lake Superior Geology Student Research Fund grant to Y.Z. Permits for  
582 fieldwork and sampling from the Minnesota Department of Natural Resources are grate-  
583 fully acknowledged. We thank James Pierce and Blake Hodgin for assistance in the field.  
584 We thank Stephen Self for providing constructive comments regarding mafic lava flow  
585 volumes. We thank John Grimsich and Tim Teague at UC Berkeley EPS department  
586 for their help with petrographic sample preparation and analyses. Paleomagnetic data  
587 associated with this study are available within the MagIC database (<https://earthref.org/MagIC/17089/26d9073f-2447-4f46-85fb-8596ce5b3aab>) and all data are within  
588 a Github repository associated with this work ([https://github.com/Swanson-Hysell-Group/2021\\_AX\\_BD](https://github.com/Swanson-Hysell-Group/2021_AX_BD)) that is also archived on Zenodo (insert URL after revisions). This  
589 repository also contains Python code related to calculations, visualizations and statis-  
590 tical tests discussed herein.  
591

Table 1:  
 Summary of new site level paleomagnetic data for the Beaver River diabase and anorthosite xenoliths. n/N: number of samples/sites analyzed and included in the site/grand mean;  $dec_{is}$  &  $inc_{is}$ : in situ mean declination and inclination for the site;  $dec_{te}$  &  $inc_{te}$ : tilt-corrected mean declination and inclination for the site; k: Fisher precision parameter; R: resultant vector length;  $\alpha_{95}$ : 95% confidence limit in degrees; VGP lat.—latitude of the virtual geomagnetic pole for the site; VGP lon—longitude of the virtual geomagnetic pole for the site. Full measurement level data are available within the MagIC database. <https://earthref.org/MagIC/17102/400e0fb3-a79b-42bd-aaeb-9005d2a3b488>.

site	lat	lon	n/N	$dec_{is}$	$dec_{te}$	$inc_{is}$	$inc_{te}$	k	$\alpha_{95}$	VGP lat <sub>is</sub>	VGP lon <sub>is</sub>	VGP lat <sub>te</sub>	VGP lon <sub>te</sub>
AX1	47.2	-91.4	8.0	293.3	42.6	288.8	54.9	536.0	2.4	33.4	180.0	37.1	193.2
AX2	47.2	-91.4	9.0	282.0	31.3	277.4	42.6	145.0	4.3	20.4	181.8	22.6	191.1
AX3	47.6	-90.9	10.0	290.4	28.2	285.1	38.6	69.0	5.9	24.7	174.5	25.9	183.7
AX4	47.6	-90.9	7.0	291.9	20.0	288.3	30.7	91.0	6.4	22.3	169.8	24.4	177.2
AX5-10	47.6	-90.9	14.0	286.2	29.1	280.7	38.1	269.5	2.5	22.3	178.1	22.7	186.5
AX11	47.4	-91.2	8.0	284.9	23.5	281.7	35.2	305.0	3.2	19.1	176.3	22.0	184.1
AX12	47.3	-91.3	6.0	299.9	42.5	297.3	55.2	36.0	11.3	37.8	175.1	43.0	188.4
AX13	47.4	-91.2	9.0	289.8	23.0	287.3	35.1	434.0	2.5	22.2	172.4	25.7	180.0
AX14	47.3	-91.3	7.0	296.9	38.2	293.9	50.8	256.0	3.8	33.7	174.5	38.2	186.1
AX15	47.3	-91.3	8.0	282.9	42.3	275.8	53.5	86.0	6.0	26.2	187.2	27.9	199.8
AX16	47.3	-91.3	8.0	273.7	39.1	265.8	49.2	396.0	2.8	18.5	191.6	19.0	202.9
AX17	47.3	-91.3	8.0	273.6	49.8	261.6	59.6	647.0	2.2	24.3	198.3	23.7	213.5
AX18	47.3	-91.3	9.0	283.8	45.5	276.0	56.9	535.0	2.2	28.5	188.7	30.2	202.8
AX19	47.3	-91.3	8.0	293.9	35.8	290.7	48.2	65.0	2.1	30.5	175.4	34.6	186.0
AX20	47.3	-91.3	5.0	294.5	44.3	290.0	56.7	271.0	4.7	35.1	180.4	39.0	194.5
AX21	47.3	-91.3	8.0	301.7	37.7	301.7	50.5	803.0	2.0	36.7	170.4	42.1	181.7
AX22	47.4	-91.2	9.0	297.2	43.1	293.8	55.7	208.0	3.6	36.3	177.6	41.0	191.1
Anorthosite mean		17.0	289.3	36.5	284.5	48.2	55.0	4.9	28.0	179.6	30.9	190.8	
BD1	47.2	-91.4	15.0	293.1	40.9	288.8	53.2	623.0	1.5	32.4	179.0	36.1	191.6
BD2	47.6	-90.9	8.0	286.6	22.7	282.0	32.6	122.0	5.0	19.9	175.0	21.0	182.8
BD3	47.4	-91.2	8.0	286.6	29.8	282.8	41.6	212.0	3.8	22.9	177.9	25.8	186.9
BD4	47.3	-91.3	8.0	300.2	40.7	297.9	53.4	47.0	8.2	37.1	173.6	42.3	186.0
BD5	47.3	-91.3	8.0	282.7	44.8	274.8	56.0	271.0	3.4	27.4	188.9	28.9	202.6
BD6	47.3	-91.3	9.0	300.0	33.2	298.3	64.0	64.0	6.5	33.4	169.2	38.6	178.9
BD7	47.3	-91.3	7.0	292.4	53.1	285.0	65.3	305.0	3.5	38.5	189.2	41.3	208.3
BD8	47.2	-91.4	10.0	287.9	52.8	278.8	64.5	300.0	2.8	35.3	191.8	37.1	209.9
BD9	47.2	-91.3	7.0	278.2	33.8	272.3	44.6	55.0	8.2	19.0	185.7	20.4	195.6
BD10	47.4	-91.2	10.0	297.0	46.2	293.0	58.7	341.0	2.6	37.8	180.0	42.2	195.1
BD11	47.4	-91.3	8.0	296.4	41.7	293.0	54.2	429.0	2.7	35.1	177.1	39.5	189.9
BD12	47.3	-91.3	8.0	288.8	38.1	284.1	50.1	141.0	4.7	28.1	180.4	31.3	191.8
BD13	47.5	-91.1	8.0	280.4	22.4	276.9	33.6	341.0	3.0	15.6	179.2	18.0	186.7
BD15	47.7	-90.6	8.0	300.1	2.3	299.3	14.2	119.0	5.1	20.6	156.9	24.8	161.7
BD17	47.4	-91.2	8.0	295.1	28.5	292.9	41.0	550.0	2.4	28.0	170.8	32.3	179.3
Diabase mean		15.0	291.0	35.7	286.9	47.7	51.6	5.0	29.0	178.2	32.5	189.5	

593 **References**

- 594 Beck, M. E. (1970). Paleomagnetism of Keweenawan Intrusive Rocks, Min-  
 nesota. *Journal of Geophysical Research*, 75(26), 4985–4996. doi:  
 596 10.1029/jb075i026p04985
- 597 Beck, M. E., & Lindsley, N. C. (1969). Paleomagnetism of the Beaver Bay Complex,  
 598 Minnesota. *Journal of Geophysical Research*, 74(8), 2002–2013. doi: 10.1029/  
 599 jb074i008p02002
- 600 Boerboom, T. J. (2004). *M-147 Bedrock geology of the Split Rock Point quadrangle,*  
 601 *Lake County, Minnesota* (Tech. Rep.). Minnesota Geological Survey.
- 602 Boerboom, T. J., Green, J., & Albers, P. (2007). *M-174 Bedrock geology of the Lut-*  
 603 *sen quadrangle, Cook County, Minnesota* (Tech. Rep.). Minnesota Geological  
 604 Survey.
- 605 Boerboom, T. J., & Green, J. C. (2006). *M-170 Bedrock geology of the Schroeder*  
 606 *quadrangle, Cook County, Minnesota* (Tech. Rep.). Minnesota Geological Sur-  
 607 vey.
- 608 Boerboom, T. J., Green, J. C., Albers, P., & Miller, J., J.D. (2006). *M-171 Bedrock*  
 609 *geology of the Tofte quadrangle, Cook County, Minnesota* (Tech. Rep.). Min-  
 610 nesota Geological Survey.
- 611 Books, K. G., White, W. S., & Beck, M. E. (1966). *Magnetization of Keweenawan*  
 612 *gabbro in northern Wisconsin and its relation to time of intrusion.* Geological  
 613 Survey Research.
- 614 Bryan, S. E., Peate, I. U., Peate, D. W., Self, S., Jerram, D. A., Mawby, M. R., ...  
 615 Miller, J. A. (2010). The largest volcanic eruptions on Earth. *Earth-Science*  
 616 *Reviews*, 102(3-4), 207–229. doi: 10.1016/j.earscirev.2010.07.001
- 617 Cannon, W. F., & Hinze, W. J. (1992). Speculations on the origin of the North  
 618 American Midcontinent rift. *Tectonophysics*, 213(1-2), 49–55. doi: 10.1016/  
 619 0040-1951(92)90251-z
- 620 Cannon, W. F., & Nicholson, S. W. (2001). Geologic map of the Keweenaw Penin-  
 621 sula and adjacent area, Michigan. *USGS Numbered Series*, 2696.
- 622 Cherniak, D., Hanchar, J., & Watson, E. (1997, jan). Rare-earth diffusion in zircon.  
 623 *Chemical Geology*, 134(4), 289–301. doi: 10.1016/s0009-2541(96)00098-8
- 624 Cherniak, D., & Watson, E. (2001). Pb diffusion in zircon. *Chemical Geology*, 172(1-  
 625 2), 5–24. doi: 10.1016/s0009-2541(00)00233-3

- 626 Condon, D. J., Schoene, B., McLean, N. M., Bowring, S. A., & Parrish, R. R. (2015,  
627 9 1). Metrology and traceability of U–Pb isotope dilution geochronology  
628 (EARTHTIME tracer calibration part I). *Geochimica et Cosmochimica Acta*,  
629 164, 464–480. doi: 10.1016/j.gca.2015.05.026
- 630 Davis, D. W., & Paces, J. B. (1990). Time resolution of geologic events on the  
631 Keweenaw Peninsula and implications for development of the Midcontinent  
632 Rift system. *Earth and Planetary Science Letters*, 97(1-2), 54–64. doi:  
633 10.1016/0012-821x(90)90098-i
- 634 Delaney, P. (1987). *Heat transfer during emplacement and cooling of mafic dykes*.  
635 Geological Association of Canada.
- 636 Doyle, M. (2016). *Geologic and geochemical attributes of the Beaver River Diabase*  
637 *and Greenstone Flow: Testing a possible intrusive-volcanic link in the 1.1 Ga*  
638 *Midcontinent Rift* (Unpublished master's thesis). University of Minnesota.
- 639 Fairchild, L. M., Swanson-Hysell, N. L., Ramezani, J., Sprain, C. J., & Bowring,  
640 S. A. (2017). The end of Midcontinent Rift magmatism and the paleogeogra-  
641 phy of Laurentia. *Lithosphere*, 9(1), 117–133. doi: 10.1130/l580.1
- 642 Ferry, J. M., & Watson, E. B. (2007). New thermodynamic models and revised cal-  
643ibrations for the Ti-in-zircon and Zr-in-rutile thermometers. *Contributions to*  
644 *Mineralogy and Petrology*, 154(4), 429–437. doi: 10.1007/s00410-007-0201-0
- 645 Foucher, M. (2018). *Probing the Precambrian geodynamo: analysis of the geomag-*  
646 *netic field behavior and calibration of pseudo-thellier paleointensity method for*  
647 *Mesoproterozoic rocks* (Unpublished doctoral dissertation). Michigan Techno-  
648 logical University.
- 649 Green, J. C. (1982). 5: Geology of Keweenawan extrusive rocks. *Geological Society*  
650 *of America Memoirs*, 156, 47–56.
- 651 Grout, S. G. M., Frank F. (1939). The geology of the anorthosites of the Minnesota  
652 coast of Lake Superior. Minnesota Geological Survey.
- 653 Heaman, L. M., Easton, R. M., Hart, T. R., Hollings, P., MacDonald, C. A., &  
654 Smyk, M. (2007). Further refinement to the timing of Mesoproterozoic mag-  
655 matism, Lake Nipigon region, Ontario. *Canadian Journal of Earth Sciences*,  
656 44(8), 1055–1086. doi: 10.1139/e06-117
- 657 Hinze, W. J., & Chandler, V. W. (2020). Reviewing the configuration and extent  
658 of the Midcontinent Rift system. *Precambrian Research*, 342, 105688. doi: 10

- 659 .1016/j.precamres.2020.105688
- 660 Huber, N. (1973). *The Portage Lake Volcanics (Middle Keweenawan) on Isle*  
661 *Royale, Michigan* (Tech. Rep.). United States Geological Survey.
- 662 Jirsa, M. A., Boerboom, T., Chandler, V., Mossler, J., Runkel, A., & Setterholm,  
663 D. (2011). *S-21 Geologic map of Minnesota-bedrock geology* (Tech. Rep.).  
664 Minnesota Geological Survey.
- 665 Kushiro, I. (1980). Viscosity, density, and structure of silicate melts at high pres-  
666 sures, and their petrological applications. *Physics of magmatic processes*, 93-  
667 120.
- 668 Lane, A. C. (1911). The Keweenaw series of Michigan. *Michigan Geological and Bio-*  
669 *logical Survey Publication 6*, 2(4), 983.
- 670 Lawson, A. C. (1893). The anorthosites of the Minnesota Coast of Lake Superior:  
671 Geological and Natural History Survey of Minnesota. *Bulletin*, 8, 1-23.
- 672 Longo, A. A. (1984). *A correlation for a middle Keweenawan flood basalt: the*  
673 *Greenstone flow, Isle Royale and Keweenaw Peninsula, Michigan* (Unpublished  
674 master's thesis). Michigan Technological University.
- 675 Mattinson, J. M. (2005). Zircon U-Pb chemical abrasion ("CA-TIMS") method:  
676 Combined annealing and multi-step partial dissolution analysis for improved  
677 precision and accuracy of zircon ages. *Chemical Geology*, 220(1-2), 47-66. doi:  
678 10.1016/j.chemgeo.2005.03.011
- 679 McFadden, P., & McElhinny, M. (1990). Classification of the reversal test in palaeo-  
680 magnetism. *Geophysical Journal International*, 103, 725-729.
- 681 Miller, J., J.D. (1988). *M-065 Geologic map of the Silver Bay and Split Rock Point*  
682 *NE quadrangles, Lake County, Minnesota* (Tech. Rep.).
- 683 Miller, J., J.D., & Boerboom, T. J. (1989). *M-066 geologic map of the Illgen City*  
684 *quadrangle, Lake County, Minnesota* (Tech. Rep.). Minnesota Geological Sur-  
685 vey.
- 686 Miller, J., J.D., Boerboom, T. J., & Jerde, E. (1994). *M-082 Bedrock geologic map of*  
687 *the Cabin Lake and Cramer quadrangles, Lake and Cook Counties, Minnesota*  
688 (Tech. Rep.). Minnesota Geological Survey.
- 689 Miller, J., J.D., & Chandler, V. W. (1997). Geology, petrology, and tectonic signifi-  
690 cance of the Beaver Bay Complex, northeastern Minnesota. In *Middle Protero-*  
691 *zoic to Cambrian rifting, central North America*. Geological Society of Amer-

- 692                   ica. doi: 10.1130/0-8137-2312-4.73
- 693     Miller, J., J.D., & Nicholson, S. W. (2013). Geology and Mineral Deposits of the 1.1  
694        Ga Midcontinent Rift in the Lake Superior Region – An Overview. In *Field*  
695        *guide to the copper-nickel-platinum group element deposits of the lake superior*  
696        *region*. Precambrian Research Center.
- 697     Miller, J., J.D., Severson, M. J., Chandler, V. W., & Peterson, D. M. (2001). *M-119*  
698        *Geologic map of the Duluth Complex and related rocks, northeastern Minnesota*  
699        (Tech. Rep.). Minnesota Geological Survey.
- 700     Miller, J., J.D., & Weiblen, P. W. (1990). Anorthositic rocks of the Duluth Com-  
701        plex: Examples of rocks formed from plagioclase crystal mush. *Journal of*  
702        *Petrology*, *31*(2), 295–339. doi: 10.1093/petrology/31.2.295
- 703     Morrison, D. A., Ashwal, L. D., Phinney, W. C., Shih, C.-Y., & Wooden, J. L.  
704        (1983). Pre-Keweenawan anorthosite inclusions in the Keweenawan Beaver Bay  
705        and Duluth Complexes, northeastern Minnesota. *Geological Society of America*  
706        *Bulletin*, *94*(2), 206. doi: 10.1130/0016-7606(1983)94<206:paiitk>2.0.co;2
- 707     Paces, J. B., & Miller, J., J.D. (1993). Precise U-Pb ages of Duluth Complex and  
708        related mafic intrusions, northeastern Minnesota: Geochronological insights  
709        to physical, petrogenetic, paleomagnetic, and tectonomagmatic processes as-  
710        sociated with the 1.1 Ga Midcontinent Rift System. *Journal of Geophysical*  
711        *Research: Solid Earth*, *98*(B8), 13997–14013. doi: 10.1029/93jb01159
- 712     Remond, G., Cesbron, F., Chapoulie, R., Ohnenstetter, D., Roques-Carmes, C.,  
713        & Schvoerer, M. (1992). Cathodoluminescence applied to the microchar-  
714        acterization of mineral materials: a present status in experimentation and  
715        interpretation. *Scanning microscopy*, *6*(1), 2.
- 716     Rubatto, D. (2002). Zircon trace element geochemistry: partitioning with garnet and  
717        the link between U-Pb ages and metamorphism. *Chemical Geology*, *184*(1-2),  
718        123–138. doi: 10.1016/s0009-2541(01)00355-2
- 719     Schaltegger, U., Fanning, C. M., Günther, D., Maurin, J. C., Schulmann, K., &  
720        Gebauer, D. (1999). Growth, annealing and recrystallization of zircon  
721        and preservation of monazite in high-grade metamorphism: conventional  
722        and in-situ U-Pb isotope, cathodoluminescence and microchemical evi-  
723        dence. *Contributions to Mineralogy and Petrology*, *134*(2-3), 186–201. doi:  
724        10.1007/s004100050478

- 725 Schmitz, M. D., Bowring, S. A., & Ireland, T. R. (2003). Evaluation of Duluth  
726 Complex anorthositic series (AS3) zircon as a U-Pb geochronological stan-  
727 dard: new high-precision isotope dilution thermal ionization mass spectrom-  
728 etry results. *Geochimica et Cosmochimica Acta*, 67(19), 3665–3672. doi:  
729 10.1016/s0016-7037(03)00200-x
- 730 Schoene, B., Crowley, J. L., Condon, D. J., Schmitz, M. D., & Bowring, S. A.  
731 (2006). Reassessing the uranium decay constants for geochronology using  
732 ID-TIMS U–Pb data. *Geochimica et Cosmochimica Acta*, 70(2), 426–445. doi:  
733 10.1016/j.gca.2005.09.007
- 734 Self, S., Jay, A., Widdowson, M., & Keszthelyi, L. (2008). Correlation of the Deccan  
735 and Rajahmundry Trap lavas: Are these the longest and largest lava flows on  
736 Earth? *Journal of Volcanology and Geothermal Research*, 172(1-2), 3–19. doi:  
737 10.1016/j.jvolgeores.2006.11.012
- 738 Shank, S. G. (1989). The petrology of the Beaver Bay Complex near Silver Bay,  
739 northeastern Minnesota. *Minnesota, University of Minnesota*.
- 740 Sun, S.-S., & McDonough, W. F. (1989). Chemical and isotopic systematics of  
741 oceanic basalts: implications for mantle composition and processes. *Geological  
742 Society, London, Special Publications*, 42(1), 313–345. doi: 10.1144/gsl.sp.1989  
743 .042.01.19
- 744 Swanson-Hysell, N. L., Hoaglund, S. A., Crowley, J. L., Schmitz, M. D., Zhang,  
745 Y., & Miller, J. D. (2020). Rapid emplacement of massive Duluth Com-  
746 plex intrusions within the North American Midcontinent Rift. *Geology*. doi:  
747 10.1130/g47873.1
- 748 Swanson-Hysell, N. L., Maloof, A. C., Weiss, B. P., & Evans, D. A. D. (2009).  
749 No asymmetry in geomagnetic reversals recorded by 1.1-billion-year-old Ke-  
750 weenawan basalts. *Nature Geoscience*, 2(10), 713–717. doi: 10.1038/ngeo622
- 751 Swanson-Hysell, N. L., Ramezani, J., Fairchild, L. M., & Rose, I. R. (2019). Failed  
752 rifting and fast drifting: Midcontinent Rift development, Laurentia’s rapid mo-  
753 tion and the driver of Grenvillian orogenesis. *GSA Bulletin*, 131(5-6), 913–940.  
754 doi: 10.1130/b31944.1
- 755 Tauxe, L., Shaar, R., Jonestrask, L., Swanson-Hysell, N. L., Minnett, R., Koppers,  
756 A. A. P., ... Fairchild, L. (2016). PmagPy: Software package for paleomag-  
757 netic data analysis and a bridge to the Magnetics Information Consortium

- 758 (MagIC) Database. *Geochemistry, Geophysics, Geosystems*, 17(6), 2450–2463.  
759 doi: 10.1002/2016gc006307
- 760 Unsworth, J., & Duarte, F. J. (1979). Heat diffusion in a solid sphere and Fourier  
761 theory: An elementary practical example. *American Journal of Physics*,  
762 47(11), 981–983. doi: 10.1119/1.11601
- 763 van Hinsbergen, D. J. J., Steinberger, B., Doubrovina, P. V., & Gassmöller, R.  
764 (2011). Acceleration and deceleration of India-Asia convergence since the  
765 Cretaceous: Roles of mantle plumes and continental collision. *Journal of*  
766 *Geophysical Research*, 116(B6). doi: 10.1029/2010jb008051
- 767 Vervoort, J. D., Wirth, K., Kennedy, B., Sandland, T., & Harpp, K. S. (2007). The  
768 magmatic evolution of the Midcontinent rift: New geochronologic and geo-  
769 chemical evidence from felsic magmatism. *Precambrian Research*, 157(1-4),  
770 235–268. doi: 10.1016/j.precamres.2007.02.019
- 771 White, W. (1960). The Keweenawan lavas of Lake Superior, an example of flood  
772 basalts. *American Journal of Science*, 258, 367–374.